A CFD-supported dynamic system-level model of a sodium-cooled billboard-type receiver for central tower CSP applications

A CFD-supported dynamic system-level model of a sodium-cooled billboard-type receiver for central tower CSP applications

M. Cagnoli[a], A. de la Calle[b], J. Pye[c], L. Savoldi[a], R. Zanino[a,*]

[a] *Dipartimento Energia, Politecnico di Torino, C.so Duca degli Abruzzi 24, 10129 Torino, Italy*
[b] *CSIRO Energy, 10 Murray Dwyer Ct, Mayfield West, NSW 2304, Australia*
[c] *Australian National University (ANU), Canberra, Australia*

* Corresponding author: roberto.zanino@polito.it

Abstract

This work focusses on the dynamic modeling of a sodium-cooled billboard-type receiver, as adopted in the reference plant of this study, the Jemalong Solar Thermal Station, in Australia. A detailed system-level thermal-fluid-dynamic model is developed in the OpenModelica framework, with the aim to predict the receiver behavior during transients, as well as its performance upon reaching steady-state conditions. The model solves the conjugate heat transfer problem relating conduction in the receiver pipes to the internal flow of sodium. The convective losses from the irradiated face of the receiver, due to the external flow of air, are calculated using empirical correlation available in literature for flat-plates and then carefully evaluated using 3D Computational Fluid Dynamics (CFD), which allows taking into account the actual geometry of the receiver. The CFD results, considering different wind speeds and highlighting the cavity-like effects of the receiver geometry under consideration, are first compared with those obtained from empirical correlations available in the literature for vertical plates in the case of uniform temperature distribution on the absorber pipes, showing significant differences. Then an iterative coupling procedure with the system-level model of the same receiver is proposed, which facilitates handling of the more realistic case of a non-uniform temperature distribution. Finally, we present and discuss the successful benchmark in a simple case of the system-level model against another model from the literature, its preliminary validation against experimental data, and first applications to a fast start-up/passing cloud/shut-down transient and to a whole-day simulation with controls.

Keywords: central tower systems, billboard-type receiver, sodium, dynamic model, Modelica, CFD

1 Background and motivation

Concentrated solar power (CSP) has great potential to become an effective alternative to fossil-fuel based power plants. This is due to the immense solar resource available, which exceeds the current world's energy demand several thousand times (Abbott, 2010). Furthermore, CSP plants, in contrast to photovoltaic (PV) plants, can efficiently store thermal energy, allowing electricity dispatch according to energy demand.

Most of the CSP plants currently under operation are based on the parabolic trough (PT) collector technology that was established at commercial level in the 1980s (SEGS plants in California, USA) (Kolb, 1994). However, the current overall efficiency reached by this technology is about 15-16% and the outlook for significant improvements is limited (Behar et al., 2013). The solar-to-electricity efficiency has to be significantly improved to make CSP

generation competitive with the fossil fuel or nuclear-based technology. For this reason, central receiver systems have been proposed, in which a large heliostat field concentrates the sunlight onto a central receiver, typically of a tubular type and located on the top of a tower, which transfers the incident energy to the heat transfer fluid. These systems have a concentration ratio higher than the PT and can be operated at very high temperatures (> 1000 °C) (Ávila-Marín, 2011). This leads to higher thermodynamic cycle efficiencies downstream of the receiver, which improves the overall plant performance. Other advantages of the central receiver technology include the possibility to directly drive a Brayton cycle if a gaseous heat transfer fluid is adopted, and the easy hybridization with fossil-fuel power plants. Moreover, Behar et al. (2013) indicated that this technology has great potential for cost reduction and efficiency improvements.

The exploitation of this potential requires the adoption of suitable heat transfer fluids (HTFs), which must be stable at high temperature. Currently, the state-of-the-art HTFs for tubular central receivers are molten salts, which, however, cannot reach very high temperatures. Liquid metals are promising candidates as HTFs due to their high boiling point and thermal conductivity. Among the liquid metals, sodium is the most technologically mature potential HTF, as it has been the focus of research in the nuclear field for the liquid metals fast breeder reactors (Cochran et al., 2010).

An exergy analysis was conducted in a recent study (Pye et al., 2015) to estimate the thermal performance of a tubular receiver using different HTFs, namely liquid sodium, molten salts, supercritical CO2 and ideal air. First, the selected working fluids were compared at equivalent temperatures range 300-550 °C. Liquid sodium had the best exergy efficiency, which, however, was very close to the one of the molten salts. The benefit of using sodium became more evident when the operating range was extended up to 850 °C, which is safely below the sodium boiling temperature, and the concentration ratio was doubled. Doubling the concentration ratio halves the receiver absorber surface without changing the amount of incident energy. In these conditions, Pye et al. (2015) determined a significant increase in the exergy efficiency, when moving from molten salts (54.2%) to liquid sodium (63.2%).

A comprehensive comparison between sodium and a molten salt commonly used in CSP applications, Hitec ®, is presented in Boerema et al. (2012). This study concluded that using liquid sodium as an HTF has a number of advantages. First, sodium has a larger operating temperature range, both at the lower limit (a melting temperature of 97.7 °C vs. 142 °C) and at the upper limit (a boiling temperature of 873 °C vs. the Hitec upper usability limit of 535 °C). Second, the sodium thermal conductivity is two orders of magnitude higher than that of Hitec, resulting in a significantly higher convective heat transfer coefficient (approximately an order of magnitude higher than Hitec). The high sodium heat transfer coefficient helps to lower the wall temperature on the irradiated tube side. This in turn reduces the circumferential temperature gradient that is the main cause of the stresses in an absorber tube, as observed in (Logie et al., 2018). As a result, an increase in the concentration ratio and consequently a reduction of the receiver absorber surface is made possible. This was quantified to be approximately 57% (Boerema et al., 2012). The main disadvantages in using sodium instead of molten salts are the higher cost (up to 200% more expensive per kilogram) and safety issues. Sodium, at temperatures commonly reached in CSP applications, spontaneously ignites when exposed to air. If this occurs, water cannot be used as an extinguishing medium, as sodium reacts violently with water. A sodium spray fire accident occurred at the PSA in 1986, which led to the end of the sodium receiver experiments and contributed to slowing down the research in this field (Coventry et al., 2015; Romero and González-Aguilar, 2017). In addition, molten salts can be effectively used both as a heat transfer fluid and as a storage medium, unlike sodium. In the case of sodium, a sensible one-tank thermocline system with filler material has been identified as the most promising currently-available concept (Niedermeier et al., 2016).

In the CSP field, there have been a limited number of experiences with sodium as HTF, mostly in Spain and in the USA (Coventry et al., 2015). In 1977, the Small Solar Power Systems (SSPS) project of the International Energy Agency (IEA) was established, which aimed at developing and testing at the Plataforma Solar de Almeria (PSA) two sodium-cooled central receivers (Coventry et al., 2015; IEA, 1986). The first receiver was a 2.8 MWt semi-cavity receiver operated during 1981-1983, while the second one was a 2.5 MWt external billboard receiver that was tested during the years 1983-1984; both these receivers were designed to heat the liquid sodium from 270 °C (inlet temperature) to 530 °C (outlet temperature). The conclusions of the SSPS project indicated that the external receiver performed better than the semi-cavity one, being the measured daily average efficiency 91.9% and 77.4%

respectively (IEA, 1986). The reasons for this difference were identified in the higher heat flux in the external receiver (1.4 versus 0.63 MW/m^2) and in the higher surface of the semi-cavity receiver exposed to heat losses.

In the same years of the SSPS project (early 1980s), a sodium-cooled external tubular test receiver was installed at the Central Receiver Test Facility in New Mexico (USA), to prove the maturity of the sodium as HTF in CSP applications (Coventry et al., 2015; Rockwell International, 1983). The receiver was designed to heat the sodium up to 593 °C starting from an inlet temperature of 288 °C and it operated with heat fluxes up to ≈ 1.5 MW/m^2. The receiver efficiency determined during the test sessions ranged between 90% and 96%; no control issues or major problems at the plant subsystems were detected during this experimental campaign.

Recently, the Jemalong Solar Thermal Station (JSTS), a sodium-cooled 1.1 MWe central tower pilot plant with 5 solar fields/towers developed by Vast Solar (Vast Solar, 2018), rated at 1.1 MWe with 3 h thermal energy storage, has been commissioned in Forbes, New South Wales, Australia and will be considered as the reference plant for this work, see Figure 1a. Each receiver adopts a billboard-type sodium-cooled receiver, see Figure 1b, made of an array of parallel circular pipes separated by a tiny gap (≈ 1mm). The pipes are connected through an inlet and an outlet manifold. Just the front side of the tube bank is irradiated, while the back side is protected by an external shell against radiative and convective losses. Further data provided directly by Vast Solar about the receiver geometry (pipes length, diameter, etc.) cannot be disseminated here since they are confidential.

(a) (b)

Figure 1 – Jemalong Solar Thermal Station, (a) aerial view of the whole plant and (b) solar receiver

In view of the above, there is a clear interest to predict the behavior of such a receiver during transient operation, both to test different control strategies and to assist in the assessment of possible lifetime reduction issues related to thermal fatigue. Partly motivated by that, the SolarTherm Modelica library is under development as an ASTRI project (De la Calle et al., 2017; Scott et al., 2017). It includes components for the heliostat field, the thermal storage, the power block, the control system, and the receiver ; see Figure 2. The receiver model is relatively simple, with the whole absorber tube approximated by a single control volume, while the incident heat is assumed to be evenly distributed across the tubes. Fluid properties are evaluated at the center of the control volume assuming a linear temperature distribution between the inlet and outlet section. The thermal resistance offered by the tube wall, as well as its thermal capacity, are neglected in this simple model; this means that the radiative losses are estimated considering the average fluid temperature instead of the outer surface temperature of the pipe wall. Convective losses are not calculated. In conclusion, this simple receiver model is suitable for annual simulations, but it cannot predict the receiver temperature distribution and therefore it cannot be used for high-accuracy transient simulations.

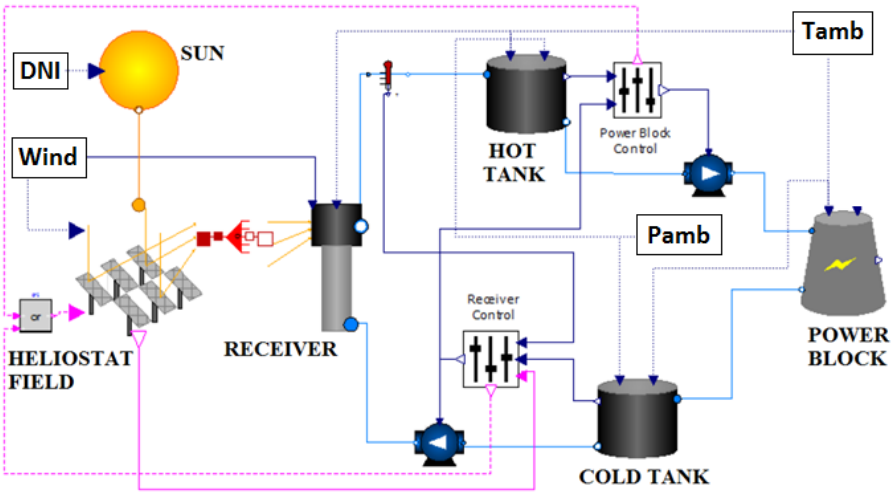

Figure 2 – System level simulation environment provided in the SolarTherm library

The present work focuses on the development of a dynamic model of a sodium-cooled billboard-type receiver for the evaluation of its thermal performance. The model uses as an input the 2D incident heat flux distribution and is aimed at computing the evolution of the temperature distribution in the different receiver components (sodium, pipes), while simultaneously providing, thanks to the support of a detailed CFD approach, a careful estimate of the (radiative and convective) heat loss distribution along each pipe of the tube bank. Finally, the model should be useful for fast, system-level analyses with SolarTherm aimed to the evaluation of different control strategies.

The paper is organized as follows: first, the system-level model is presented (Section 2); then, the CFD model is introduced (Section 3), which is exploited to accurately simulate the external air flow. The convective heat losses determined by the CFD model are discussed in the case of uniform surface temperature (CFD alone) and in the case in which the incident heat is imposed (CFD model coupled with the system-level model). In Section 5, a benchmark with a similar model available in the literature and a preliminary validation against experimental data are performed to prove the reliability of the system-level model. This is then used to simulate a fast transient (start-up, passing cloud, shut-down) and a whole day plant operation. The latter considers all the major sub-systems of the CSP plant.

2 System-level model

The model, as shown in Figure 3 and Figure 4, focusses on the heat transfer between the directly irradiated side of the pipe wall and the internal flow of sodium with a single-pass flow pattern, while the external flow of air is lumped in a suitable convective heat transfer coefficient (HTC).

2.1 Model discretization

3D transient heat conduction in each pipe wall, ignoring inter-pipe heat transfer, is approximated as follows:

- A coarse azimuthal discretization is adopted (irradiated front side plus adiabatic back side) and negligible azimuthal heat conduction is assumed (Rodríguez-Sánchez et al., 2014), see Figure 3.
- A coarse radial discretization is adopted (midpoint plus 2 interface nodes) and heat flux continuity at interfaces is assumed (Zhang et al., 2013), see Figure 4;
- The axial direction is discretized in a selected number *N* of uniformly distributed segments.

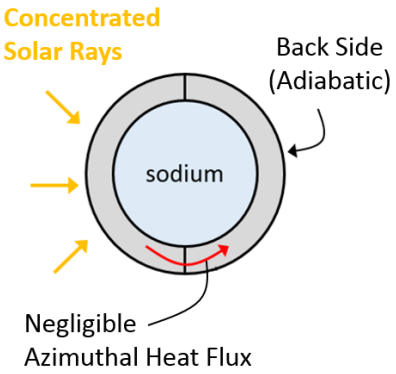

Figure 3 – System-level model, sketch view of a tube cross section with the main assumption (adiabatic back wall and negligible azimuthal heat flux) highlighted.

To check a-priori that the assumption of negligible azimuthal conduction is reasonable, a simplified calculation has been performed based on the results obtained by Boerema et al. (2013), which indicates that azimuthal conduction accounts for less than 1% of the heat transferred by radial conduction.

The 1D (axial) dynamic mass and energy balances for the Na are approximated and solved using the same discretization introduced above for the axial heat conduction in the pipes.

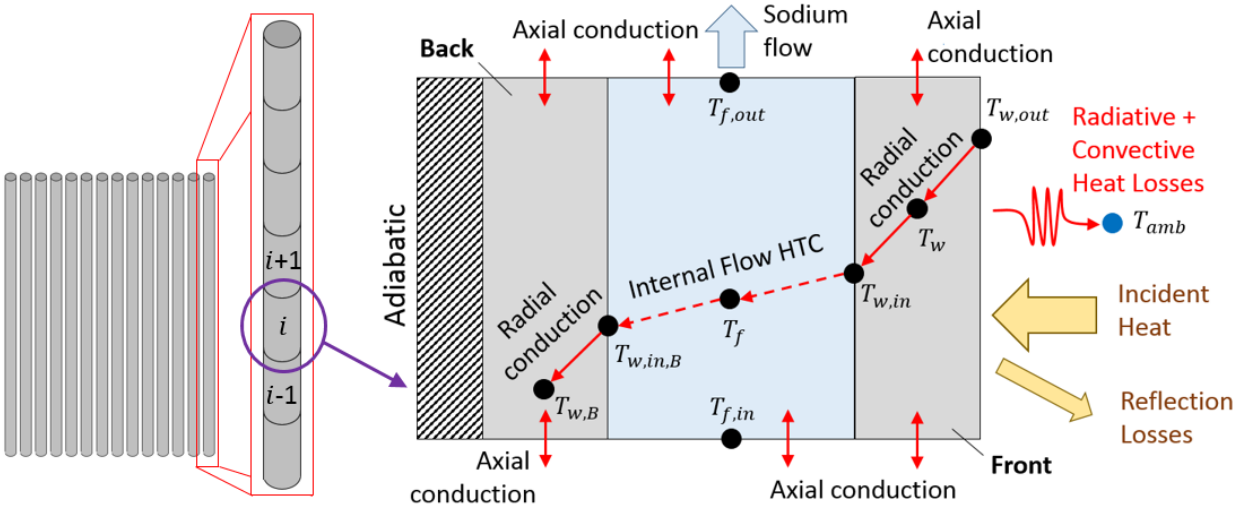

Figure 4 – System-level model, sketch of a tube longitudinal section with the radial and axial heat fluxes computed by the model.

The model has been implemented in Modelica, which is a non-proprietary, object-oriented, equation based language to conveniently describe complex physical systems containing, e.g., mechanical, electrical, hydraulic, thermal, control, electric power or process-oriented subcomponents (Modelica Association, 2018). It may be worthwhile to notice that several authors have been using Modelica within the context of CSP modeling, see e.g. (Edman and Windahl, 2015; Zhang et al., 2013).

The above-mentioned models are presented in detail in the following sub-sections.

2.2 Heat conduction in the pipes

Both the front and back wall are discretized along the pipe axis and the subscript i is used here to indicate the i-th element along the pipe axis (Figure 4). To account for thermal inertia, we consider the whole thermal mass to be lumped at the midpoint of the wall thickness, as done for instance in the dynamic model developed by Zhang (Zhang et al., 2013).

The governing energy balance equation (partial differential equation) is provided in Eq. 1a.

$$\rho_w \left(\frac{1}{2} dV_w\right) c_{p,w} \frac{dT_w}{dt} = k\left(\pi \frac{D_o^2 - D_i^2}{4} dx\right) \frac{\partial^2 T_w}{\partial x^2} - k(2\pi r) dx \frac{\partial T}{\partial r} \tag{1a}$$

where ρ_w and $c_{p,w}$ are the wall density and specific heat, respectively, while V_w is the volume of the pipe wall and T_w is the corresponding temperature in the center of the pipe thickness. The factor of one half is introduced in Eq. 1, as well as in Eqs. 2, 3 and 4, to take into account that only half of the pipe wall is considered here. The integration of the 3D heat conduction equation over the i-th control volume (CV) of the axial discretization of the irradiated side of the pipe wall gives the discretized energy balance (Eq. 1b).

$$\rho_w \left(\frac{1}{2} V_{w,i}\right) c_{p,w} \frac{dT_{w,i}}{dt} = Q_{ax,i} + Q_{r,out,i} - Q_{r,in,i} \tag{1b}$$

The right hand side of Eq. 1a takes into account the heat conduction along the axial and the radial direction, which corresponds, in Eq. 1b, to the integrated terms Q_{ax} and Q_r, respectively. The former ($Q_{ax,i}$) is the net heat source in the i-th element due to conduction along the pipe axis

$$Q_{ax,i} = \frac{1}{2} k \left(\frac{D_o^2 - D_i^2}{4} \pi\right) \frac{T_{w,i-1} - 2T_{w,i} + T_{w,i+1}}{\Delta x} \tag{2}$$

where k is the solid thermal conductivity (assumed here to be constant), Δx is the uniform axial mesh size, while D_o and D_i are the pipe outer and inner diameter, respectively.

$Q_{r,out,i}$ is the net heat source due to radial conduction between the outer surface of the pipe and the middle section, whose diameter is indicated as D_m in Eqs. 3 and 4. Note that the average temperature between the inner and outer surface of the pipe wall is not exactly reached in the middle of the pipe thickness due to the non-linear radial temperature profile. However, this simplification, which for instance was adopted also in the ThermoPower Modelica library (Casella and Leva, 2006), should cause a small error since the deviation between the average temperature and the temperature in the mid-point has been checked to be really modest (< 2°C).

$$Q_{r,out,i} = \frac{1}{2} k (2\pi \Delta x) \frac{T_{w,out,i} - T_{w,i}}{\ln(D_o/D_m)} \tag{3}$$

while $Q_{r,in,i}$ is the net heat source due to radial conduction between the middle of the pipe wall and the inner surface (see Figure 4).

$$Q_{r,in,i} = \frac{1}{2} k (2\pi \Delta x) \frac{T_{w,i} - T_{w,in,i}}{\ln(D_m/D_i)} \tag{4}$$

Looking at the interfaces, $Q_{r,in}$ corresponds to the heat transferred to the sodium flow by convection, whereas $Q_{r,out}$ is equal to the net heat absorbed by the irradiated pipe considering the optical and thermal (convective and radiative) losses, thus it corresponds to

$$Q_{r,out,i} = Q_{in,i} - Q_{refl,i} - Q_{emit,i} - Q_{conv,i} \tag{5}$$

The term Q_{in} represents the incident power, which is the thermal driver of the receiver model.
The optical losses (Q_{refl}), caused by the reflected share of the incident solar rays, are computed according to

$$Q_{refl,i} = (1 - \alpha) Q_{in,i} \tag{6}$$

where α is the absorptivity of the pipe surface coating, which is assumed to be constant.
The radiative heat losses (Q_{emit}) are calculated by means of Stefan-Boltzmann's law

$$Q_{emit,i} = \frac{2}{\pi} \cdot \varepsilon \sigma \cdot \frac{\pi}{2} D_{ext} \Delta x \cdot \left({T_{w,out,i}}^4 - {T_{amb}}^4 \right) \tag{7}$$

where the Pyromark 2500 emissivity ε is a function of the irradiated pipe wall temperature (Ho et al., 2013), which is assumed to be uniform along the pipe (half) circumference, $2/\pi$ is the view factor for adjacent pipes, σ indicates the Stefan-Boltzmann's constant ($\approx 5.67 \times 10^{-8}$) and T_{amb} is the ambient temperature.
The convective losses (Q_{conv}) can be determined as a first approximation using Newton's cooling law, considering mixed (natural plus forced) convection conditions, according to Siebers et al. (1982), as follows

$$H_{ext} = \left(H_{ext,n}^{3.2} + H_{ext,f}^{3.2} \right)^{1/3.2} \tag{8}$$

where $H_{ext,n}$ is the heat transfer coefficient for free (natural) convection, given in Siebers et al. (1985) as

$$H_{ext,n} = (k_{air}/L) \times \mathrm{Nu} = (k_{air}/L) \times 0.098 \mathrm{Gr}^{1/3} \left(\bar{T}_{w,out}/T_{amb} \right)^{-0.14} \tag{9}$$

and $H_{ext,f}$ is the heat transfer coefficient for "forced" convection (i.e., in our case, in the presence of wind), obtained from Siebers et al. (1982) as

$$H_{ext,f} = (k_{air}/L) \times \mathrm{Nu} = (k_{air}/L) \times 0.037 \mathrm{Re}^{0.8} \mathrm{Pr}^{0.6} \left(\bar{T}_{w,out}/T_{amb} \right)^{-0.4} \tag{10}$$

where k_{air} is the air heat conductivity evaluated at ambient temperature, L is the length of the absorber pipes along its axis, Nu is the Nusselt number, Gr is the Grashof number, Re and Pr are the Reynolds and Prandtl numbers respectively, while $\bar{T}_{w,out}$ is the average temperature of the pipe outer surface. These correlations are applicable for Re up to 2×10^6 and Gr up to 2×10^{12}. According to Eqs. 9 and 10, the model calculates an average heat transfer

coefficient, which is then exploited in the different control volumes along the pipe axis to compute the convective heat losses considering the temperature difference between the local outer surface pipe wall temperature and the ambient temperature. The heat transfer area corresponds to the outer pipe surface corrected by a factor $2/\pi$ that seeks to take into account that the adopted correlations were developed for flat-plate geometry.

As an alternative to this empirical approach, whose accuracy is affected a priori by the differences between the actual receiver geometry and the flat plate geometry considered in (Siebers et al., 1985, 1982), Q_{conv} can also be determined from an ad-hoc CFD analysis, as presented below in Section 3. The CFD analysis takes into account all of the relevant details of the receiver geometry under consideration, and in particular the overhang and the shell "wings".

The energy balance for the backward-facing side of the pipe wall is practically the same as that for the front wall (Eq. 1). The only relevant difference is that, since the back side is assumed to be adiabatic, the heat transferred by radial conduction between the middle section and the outer wall is imposed to be zero ($Q_{r,out} = 0$), while the radial conduction between the middle section and the inner wall and the axial conduction are computed according to Eqs. 4 and 2, respectively.

2.3 Internal sodium flow

In this Section, the conservation laws for the fluid phase are presented as implemented in the new receiver model. 1D mass, momentum and energy balance along the axis of each pipe constituting the receiver are solved, using the same 1D space discretization adopted for the pipes; the subscript *i* is again used to indicate the *i*-th control volume (CV) along the pipe axis.

The general integral form of the continuity equation for one-dimensional flow is given by

$$\frac{\partial}{\partial t}\int_{CV}\rho dV + \int_{CS}\rho\vec{U}\cdot\hat{n}dA = 0 \tag{11a}$$

where, ρ is the fluid density, dV is the elemental volume, $\vec{U}$ is the fluid velocity along the axial direction, $\hat{n}$ is the normal vector out of the control surface (CS) of elemental area dA. The second term of the equation expresses the net rate of mass through the control surface, which consists of the inlet and outlet sections of the control volume. Therefore, this term corresponds to the difference between the outlet and the inlet mass flow rate ($\dot{m}_{out,i}$ and $\dot{m}_{in,i}$ respectively).

Eq. 11a can be applied to the *i*-th CV in the form of Eq. 11b. The latter is obtained considering that the volume ΔV of the CV does not change element by element since a uniform discretization is adopted, while the time derivative of the density is computed at the outlet of the CV to avoid the occurrence of non-physical effects in the numerical solution of the algebraic system (Casella and Leva, 2006).

$$\Delta V\frac{d\rho_{out,i}}{dt} + \dot{m}_{out,i} - \dot{m}_{in,i} = 0 \tag{11b}$$

The simplified steady momentum balance equation considered here is

$$p_{out} - p_{in} = f\frac{1}{2}\frac{L}{D_i}\frac{\dot{m}^2}{\rho_{in}A^2} \tag{12}$$

where p_{out} and p_{in} are the pressure at the outlet and inlet section respectively, L is the pipe length, D_i is the inner diameter of the pipe, A is the flow cross-section, ρ_{in} is the density at the inlet section, $\dot{m}$ is the average mass flow rate in the pipe and f is Darcy's friction factor. The latter is calculated by means of Haaland's correlation (Haaland, 1983), being the sodium flow turbulent, according to the estimated Reynolds number ($Re > 10^4$).

The momentum balance equation (Eq. 12) neglects the gravity effect, which should be largely compensated by the descending branch of the sodium circuit (not included in reference simulation environment shown in Figure 2), and the kinetic term, which is expected to be modest due to the limited changes in the density. Eq. 12 is not solved for each CV, but for the pipe as a whole, considering the fluid properties at the inlet section (to simplify the model initialization). These simplifications allow a reduction in the computational cost and are justified by the fact that the pressure drop along the receiver is likely to be negligible compared with the overall pressure drop in the rest of the hydraulic circuit. Specifically, the pressure drop computed by the model in steady-state conditions is about 50 Pa, and no relevant differences have been detected computing the pressure drop using the fluid properties at the outlet section (± 3 Pa). Moreover, the sodium properties are assumed to be function only of the temperature (i.e. they do not depend on the pressure); thus, the computed values of the fluid properties are not affected by the approximations introduced in the computed pressure. The pressure profile along the axis of the pipe is obtained by imposing a linear decreasing trend from the inlet section to the outlet one.

Finally, the 1D sodium energy balance is

$$A\Delta x\left(\rho_{out,i}\frac{dh_{out,i}}{dt}+h_{out,i}\frac{d\rho_{out,i}}{dt}-\frac{dp_{out,i}}{dt}\right)+\dot{m}_{out,i}h_{out,i}-\dot{m}_{in,i}h_{in,i}=k_iA\frac{T_{f,i-1}-2T_{f,i}+T_{f,i+1}}{\Delta x}+q \quad (13)$$

This takes into account the enthalpy increase along each CV, the axial heat conduction in the liquid metal, the convective heat transfer with the pipe walls and the accumulation term, while the energy loss due to friction inside the pipe is assumed to be negligible, based on the above observations about pressure drop. As with the mass balance, the time derivatives of the dynamic variables here are computed at the outlet of the CV to avoid non-physical effects in the numerical solution. In Eq. 13, Δx is the length of the CV, h is the specific enthalpy, k is the thermal conductivity (a function of the fluid temperature), T_f is the fluid temperature (see Figure 4), q is the heat transferred by convection from the pipe inner wall, calculated as the sum of the front wall and back wall contributions using Newton's Law of Cooling.

The internal heat transfer coefficient (H_{int}) is determined as:

$$H_{int,i}=(k_i/D_{int})\times Nu=(k_i/D_{int})\times[5.6+0.0165(RePr)^{0.85}Pr^{0.01}] \quad (14)$$

where the Nusselt number is calculated using the Chen and Chiou correlation, which is particularly suitable in case of liquid sodium (Pacio et al., 2015) and was developed for Reynolds numbers in the range between 10^4 and 10^6. Although Eq. 14 was developed in the case of uniform heat flux, the Nusselt number correlations for liquid metals and fully developed flow in uniformly heated tubes can also be applied to non-uniformly heated cases, as proved in Marocco et al. (2016).

3 External air flow model

The receiver geometry may have a strong impact on the external air flow. The above-mentioned correlations for the external heat transfer coefficient (Nusselt number) were derived experimentally from flat-plate (or close to flat-pate) conditions which do not closely match the configuration of the receiver of interest in this study (see Figure 5). Specifically, the presence of the overhang and of the wings on the sides of the tube bank will alter the real-world convective flows around the tube bank. Here, we develop a 3D CFD model to simulate the actual air flow surrounding the receiver; the model will be used to accurately evaluate convective losses, to check the accuracy of

the available correlations, and to provide a tool to eventually develop ad-hoc correlations. The geometric of the present receiver is anticipated to lead to heat loss behaviour somewhere between that of an external receiver and a cavity receiver.

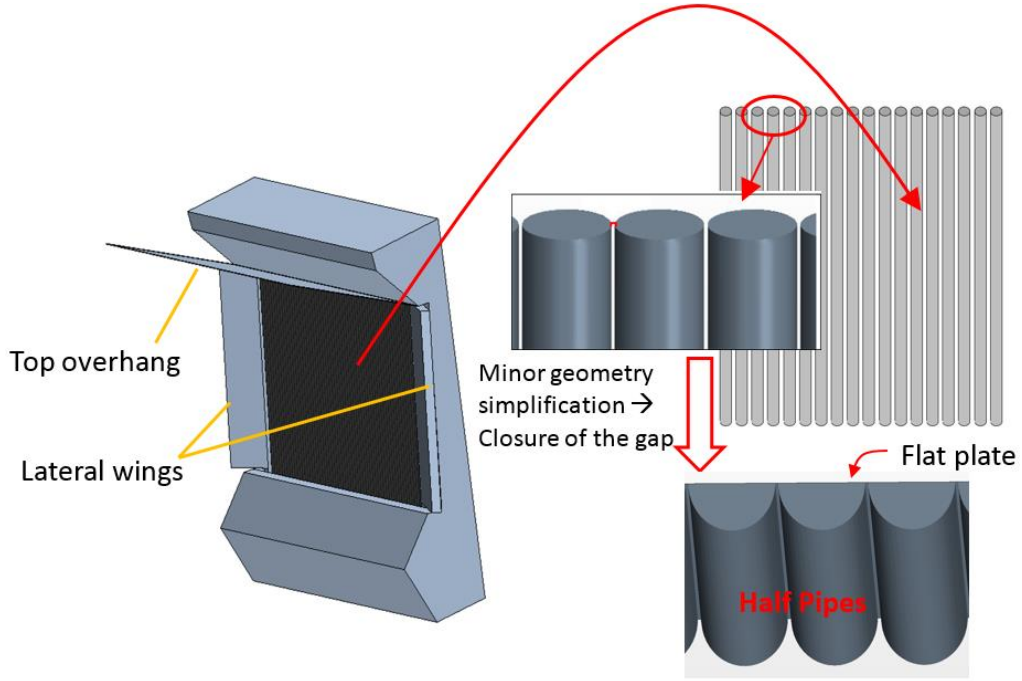

Figure 5 – 3D CAD view of the JSTS receiver with the detail of the tube bank. An enlarged view of the tube bank is also provided to show the tiny gap between the tubes, which have been removed in the CFD model for the sake of simplicity.

We adopt a 3D steady state RANS-type model with buoyancy effects considered, as implemented in the STAR-CCM+ commercial CFD code. The SST k-ω turbulence closure has been chosen, based on previous work (Torres et al., 2018; Zanino et al., 2013). Specifically, Torres et al. (2018) compared three different turbulence models (k-ε, Launder Sharma k-ε and Shear-Stress Transport k-ω) against experimental data considering the heat transfer in both forced and mixed convection conditions from a heated rectangular cuboid to the external ambient, concluding that the k-ω model well reproduce the validation data.

3.1 Computational domain and boundary conditions

In order to provide an adequate description of the air flow around the receiver, a significant volume must be included in the domain, as shown in Figure 6a. The respective boundary conditions are also indicated in the same figure, as well as the wind direction considered in the parametric study of the convective loses varying the wind speed, which is the direction parallel to the ground and symmetric with respect to the receiver face (frontal direction). This symmetry allows a significant reduction of the computational cost, by cutting in half the computational domain, although most of the figures and results below refer to the full receiver, for the sake of clarity. Atmospheric data (Australian Government – Bureau of Meteorology, 2018) close to the JSTS (Forbes) indicate that the dominant wind direction is SW, although the contribution from different directions is not negligible; see Figure 6b. The effects of different wind directions are presented and discussed in section 4.1.3.

The actual geometry of the receiver is modeled with all details (overhang, wings, etc.), except that the tiny gap between neighboring pipes has been closed, so that no air flow is allowed through the flat plate (Figure 5). The

effect of this simplification should not affect the computed heat transfer in a significant way; in fact, the back side of the receiver is insulated and it is not exposed to the external ambient. Moreover, an ad-hoc CFD simulation has been performed in order to estimate the air mass flow rate actually able to pass through the gap in the case of frontal wind, which results to be less than 2% of the incident air flow. This is because the gap between the tubes is much smaller than the tube diameter (the ratio between the two is about 1/27). Therefore, the air behind the tubes is practically trapped in the small area between the tubes and the insulation and its temperature will approach that of the tubes, leading to a negligible heat transfer by natural convection.

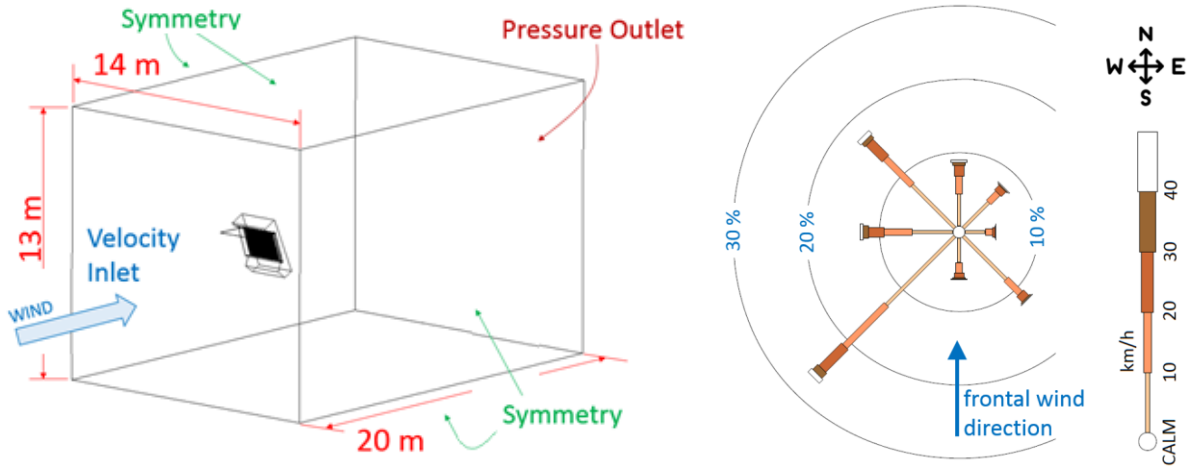

(a) (b)

Figure 6 – (a) Computational domain and boundary conditions applied on its borders and (b) wind rose close to the JSTS based on annual data collected day by day at 3 PM (Australian Government – Bureau of Meteorology, 2018) with the frontal wind direction illustrated in (a) highlighted

The computational domain ends on the irradiated surface of the pipes, since no internal flow is considered in this part of the model. Consequently, a boundary condition has to be imposed on the outer surface of the absorber pipes; particularly, the temperature distribution is imposed. In the standalone CFD simulations, a uniform temperature distribution of 634 °C (the maximum value computed by Boerema (Boerema et al., 2013)) is considered, while in the system-level/CFD coupled runs, the temperature distribution computed by the system-level model is provided as an input to the CFD model.

Table 1 – Summary of the external air domain dimensions and of the boundary conditions applied including the turbulence model adopted

External air domain	
Parameter	**Value**
Height [m]	13
Width [m]	14
Depth [m]	20
Boundary conditions & turbulence model	
Parameter	**Value**
Front face of the air domain*	Velocity inlet (normal to the face), magnitude in the range 0-10 m/s
Back face of the air domain	Pressure outlet
Lateral sides of the air domain	Symmetry condition
Outer surface of the absorber pipes	Imposed temperature distribution (uniform or non-uniform)
Turbulence model	SST k-ω turbulence closure

* To simulate different wind directions the receiver is rotated inside the external air domain

3.2 Computational mesh

The finite volume discretization of the computational domain is based on a subdivision into three sub-domains with different mesh sizes, see Figure 7. Cuboidal cells are used, except near the pipe wall where prism layers are adopted. The mesh independence of the solution was confirmed by varying the number of prism layers (not shown) and the cell base size of the sub-domains surrounding the receiver (indeed, only the base size of the cells in the outermost sub-domain is kept constant at 120 mm). Typically, 10 layers and a cell base size ranging from 15 to 42 mm in the sub-domains surrounding the receiver are sufficient, resulting in a mesh with about 50 million cells in total.

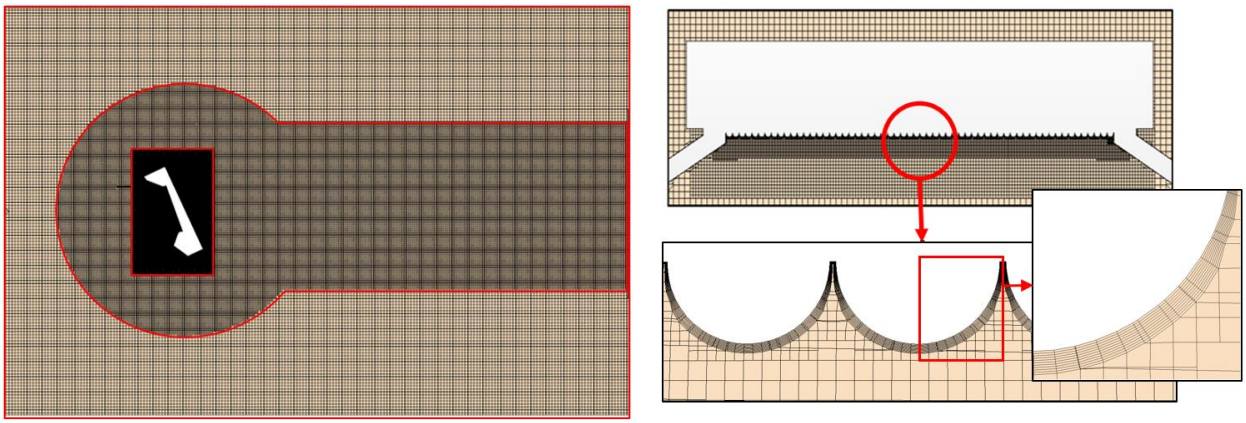

(a) (b)

Figure 7 – Example of mesh generated: (a) longitudinal cross section of the whole domain with the sub-domains highlighted by red boundaries and (b) detail of the mesh close to the receiver on a cross section perpendicular to the axis of the pipes.

4 External flow results: Assessment of the convective losses

In this section the CFD model is exploited to compute the convective losses that occur from the panel of pipes, considering both the case of imposed uniform pipe surface temperature (using the CFD model standalone), see Section 4.1, and the case of imposed incident heat flux (using the CFD model coupled with the system-level model), resulting in a non-uniform pipe surface temperature, see Section 4.2.

4.1 Imposed uniform pipe surface temperature

This section focuses on the estimation of convective losses when a uniform pipe surface temperature, equal to 634 °C, is imposed as a thermal driver. The CFD model results are first compared with those from available correlations, as a sort of validation of the model. Then the effect of different wind speeds or different wind directions is analyzed with the model.

4.1.1 Validation against available correlations

The results provided by the CFD model have been first compared with the results of the most relevant available correlations (Eqs. 8-10) that were proposed by Siebers (Siebers et al., 1982) for the case of isothermal vertical plates

in parallel horizontal flow. For that purpose, the CFD results have been post-processed in order to obtain the local heat transfer coefficient ($H_{ext,i}$) as follows

$$H_{ext,i} = \frac{\dot{Q}''_{conv,i}}{T_w - T_{amb}} \tag{15}$$

where i indicates the i-th cell of the mesh on the receiver surface, $\dot{Q}''_{conv,i}$ is the convective heat flux computed by the CFD model at the cell i, while T_w and T_{amb} are the imposed pipe wall surface and ambient temperatures. The local heat transfer coefficient can be then averaged on the receiver surface to be compared with the one obtained using the correlations.

Since the correlations proposed by Siebers apply only to the case of a vertical flat plate at uniform temperature in parallel flow, a first study has been carried out considering exactly that receiver geometry (with a wind speed equal to 5 m/s), in order to faithfully reproduce the experimental setup used by Siebers. With this setup, the HTC computed by the CFD model turns out to be very accurate, within ±2%, well within a typical error bar of experimental correlations.

We now proceed adding refinements to the simplified geometry, one by one, up to the full receiver geometry, monitoring at each step the computed HTC, as well as the product between the HTC and the heat transfer area, in order to identify how the major geometrical features of the receiver, namely the presence of

1. pipes instead of a flat surface,
2. tilting from the vertical location, and
3. addition of overhang and wings.

Table 2 – Comparison between the CFD results (different geometries) and the correlations (Eqs. 8-11) applied to the vertical smooth plate in terms of HTC and HTC multiplied by the heat transfer area, assuming a wind speed equal to 5 m/s and a uniform surface temperature (634 °C)

Case of study	**HTC [W/m^{2}K]**		**HTC × Area [W/K]**	
	CFD	**Correlation**	**CFD**	**Correlation**
Smooth vertical plate (parallel flow)	12.1	12.3	31.2	31.8
Vertical tube bank (parallel flow)	9.37	-	37.5	-
Vertical tube bank (normal flow)	9.18	-	36.7	-
Tilted tube bank (normal flow)	10.8	-	43.2	-
Actual receiver geometry (normal flow)	5.95	-	23.8	-

Looking at Table 2, which summarizes the results of our analysis in this section, the first geometry variation introduced is the surface roughness given by the presence of the pipes, while the flow direction is kept parallel. The resulting HTC decreases significantly (≈ -23%) due to the surface roughness that creates regions of very low air speed between adjacent pipes, as shown in Figure 8. On the contrary, the product between the HTC and the heat transfer area increases (≈ +20%) since the increase of the area exposed to the external ambient is larger than the reduction of the heat transfer coefficient. According to Figure 8, in the regions between two neighboring pipes a small vortex structure can be observed. These vortices provide a limited air mixing within the flow region characterized by the thermal gradient (see the temperature field in Figure 8) and, consequently, they are not able to replace the hot air close to the pipe surface with fresh (cold) air. Close to the tiny gap that separates adjacent pipes, the air is practically at rest and its temperature approaches that of the pipe surface. In addition, Figure 8 shows that the first pipe of the tube bank at the leading edge behaves like a cylinder in cross flow. Particularly, it presents a thin boundary layer (with respect to the pipe diameter) on the side exposed to the air flow that evolves up to the separation point, at about 90° from the leading edge, where the flow detachment occurs generating a wake that affects the first 5–6 pipes of the tube bank.

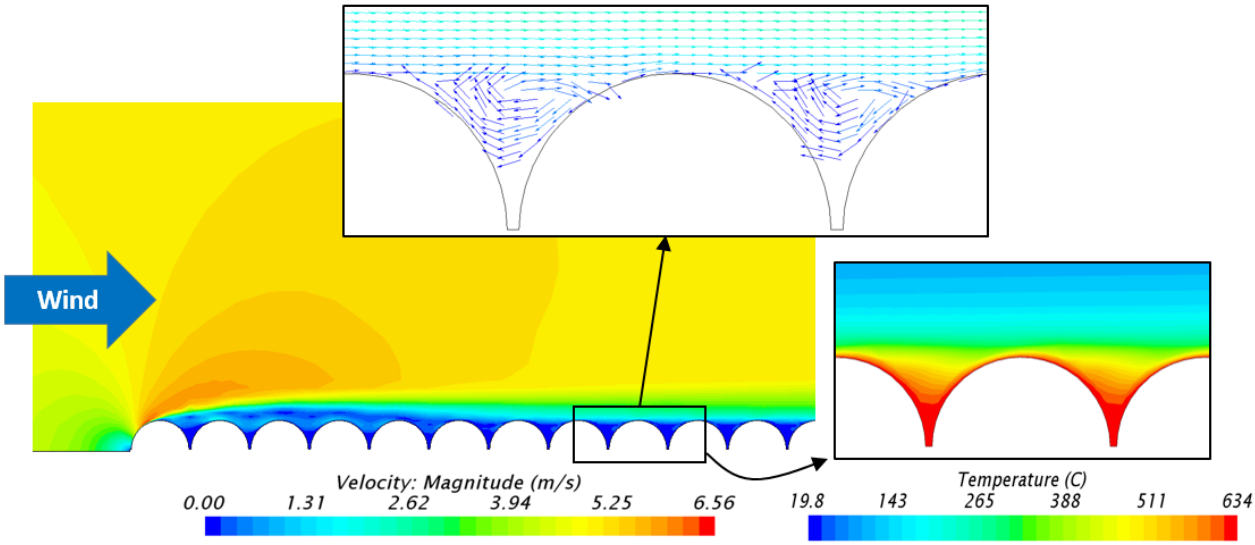

Figure 8 – Contours of air speed close to the leading edge in the horizontal mid-plane of the vertical tube bank in the case of parallel flow (wind speed set at 5/m/s). The details of the velocity vectors and of the temperature field in the region between adjacent pipes are also provided.

As a second variation, the flow direction is changed from parallel to normal to the vertical tube bank; this normal flow corresponds to the frontal wind direction defined in section 3.1. No relevant changes in the computed HTC can be observed with respect to the previous case. This is because the main air stream is divided in two symmetric branches due to the presence of the receiver, which flow almost parallel to the tube bank determining a condition similar to the one of the previous case (see Figure 9). Consequently, the flow field between adjacent pipes is again characterized by the presence of small vortices and by air at rest in the zone close to the base of the pipes, as visible in Figure 9.

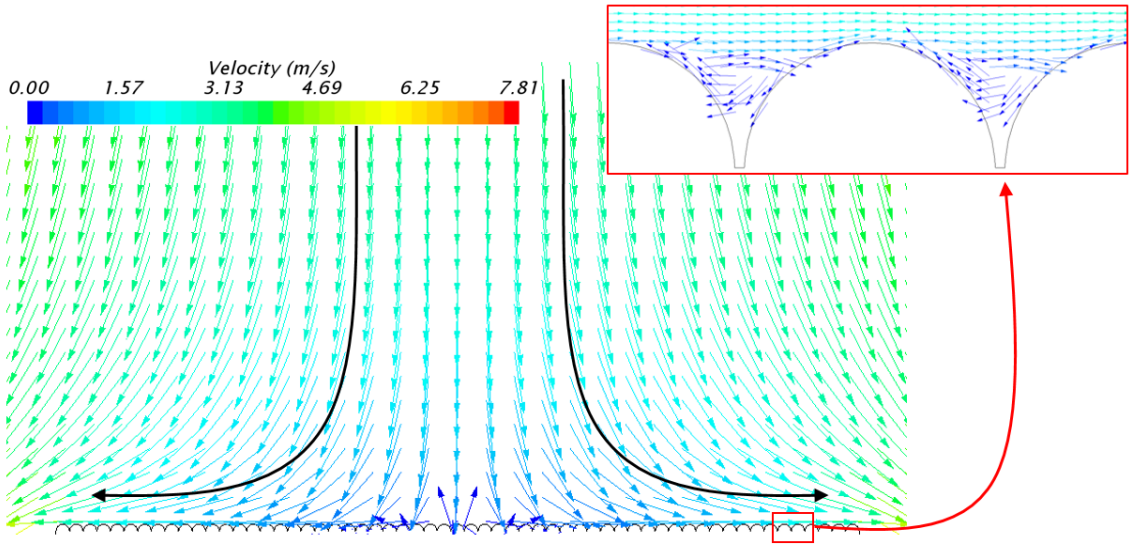

Figure 9 – Velocity vectors in the horizontal mid-plane of the vertical tube bank in the case of flow normal to the vertical tube bank (wind speed set at 5 m/s) with the zoom on the region between adjacent pipes

The flow field between adjacent pipes, presented in Figure 8 and Figure 9, could vary in the actual geometry due to the fact that the gap between the pipes is open; however, due to the counter-pressure established in the rear side of the pipes, only a negligible amount of air passes through the gap. The third variation consists in tilting the tube bank

with respect to the vertical direction. In this way, an increase of the computed HTC is obtained, which can be explained observing that the higher is the tube bank inclination, the more the pipes behave like longitudinal fins. This means that the air speed in the regions between the pipes is higher with respect to the previous cases, leading to a more effective replacing of the hot air close to the pipe surface that in turn determines a higher heat transfer by convection.

As a last variation, finally leading to the actual receiver geometry that was shown in Figure 5, the external structure, including the lateral wings and the top overhang, is introduced. The resulting HTC strongly decreases with respect to the case of the tilted tube bank (≈ -45%) with of course the same remarkable reduction of the product between the HTC and the heat transfer area that turns out to be significantly lower than the one calculated using the correlations (≈ -25%). This strong reduction of the computed HTC is due to the fact that the external structure, particularly the above-mentioned lateral wings and top overhang, effectively protects the receiver from the external air flow close to the hot absorber pipes. Figure 10a shows that the air flow is symmetrically divided in two branches, as already observed for the tube bank in the case of normal flow. However, in this case the lateral wings act as an obstacle to the air flow that leaves the receiver surface from the lateral sides, slowing down the flow at the sides of the tube bank. According to Figure 10b, the top overhang prevents the hot air from leaving the receiver from the top side; indeed, the main flow is forced by the wind along the overhang, then downwards along the receiver. At the bottom end of the pipes, the external structure presents a short overhang that partially blocks the main descending flow. Therefore, the external structure (lateral wings, the top overhang and the short bottom overhang) hinder the replacement of the hot air close to the absorber pipes with fresh air leading to cavity-like, rather than flat-plate behaviour.

In addition, Figure 10b shows that flow structures (vortices) arise near the top and the bottom end of the pipes, which are driven by the main descending flow. A quasi-stagnation point can be observed between the top vortex and the main descending flow; this is because part of the flow is sucked in the top vortex, while part of the flow goes down along the receiver and in the region where the main flow is divided the air is almost at rest.

Although a direct validation of the final receiver geometry against the correlations of Siebers is not possible, the CFD model of the actual receiver is likely to provide reliable results since it has been developed starting from a validated flat plate model, and then introducing the main geometry features step by step. For each step, reasonable results have been found, as discussed above.

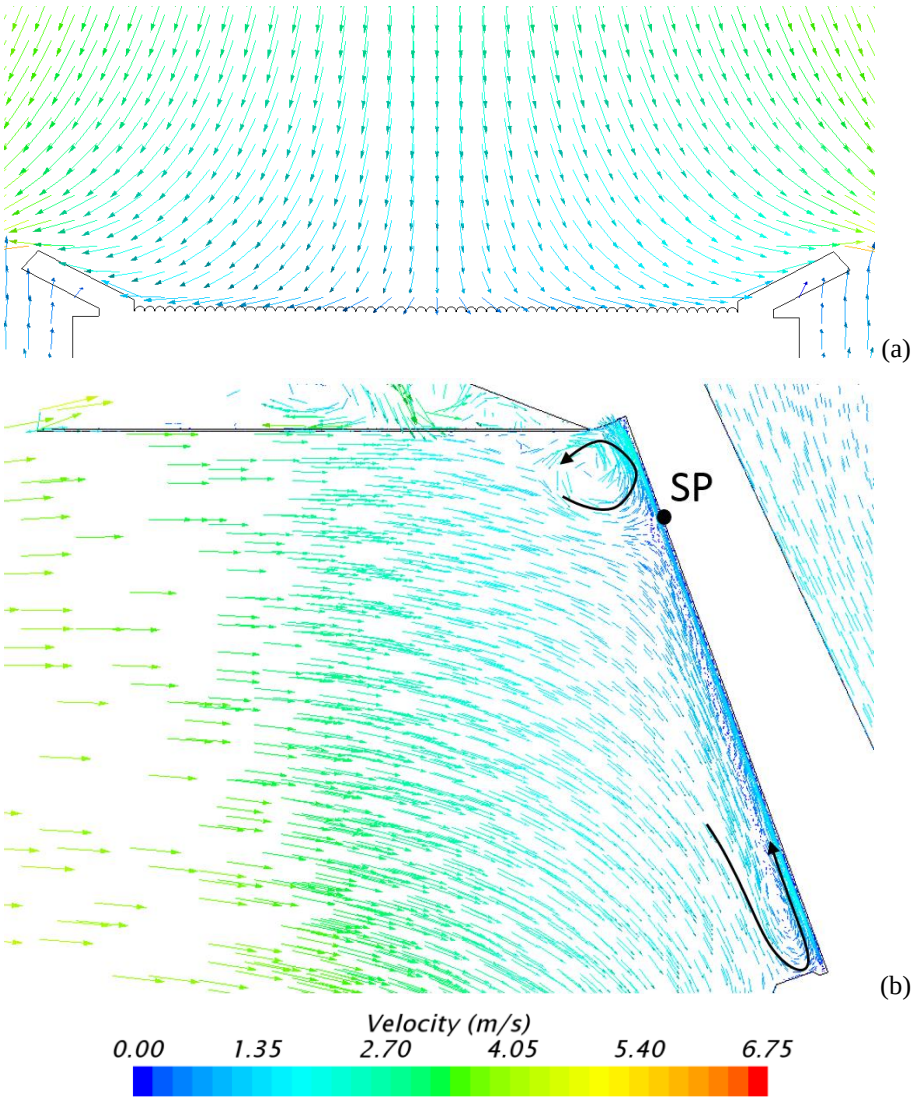

Figure 10 – Velocity vectors in the plane normal to the tubes and passing through the center of the tube bank (a) and in the vertical mid-plane with the vortices and the quasi-stagnation point (SP) highlighted (b) in the case of frontal wind (5 m/s).

Figure 11 shows the convective heat losses distribution on the receiver front face. The peaks in the convective heat flux are determined by the vortices already identified in Figure 10b, while the local minimum that occurs before of the peak in the top side is caused by the low air speed in the quasi-stagnation point. Otherwise, the convective losses are roughly uniform along most of the pipe length. The vortex structures locally enhance the heat losses between the receiver surface and the environment. This is due to the improved air mixing, which effectively replaces the heated air close to the absorber tubes with fresh air at ambient temperature. This is a feature that has been largely exploited in several engineering fields to enhance the heat transfer, see for example the work of Fiebig and Habchi (Fiebig, 1998; Habchi et al., 2012). At a smaller scale, vortices appear also between the absorber pipes, as already noticed in the previous cases (see for example Figure 9).

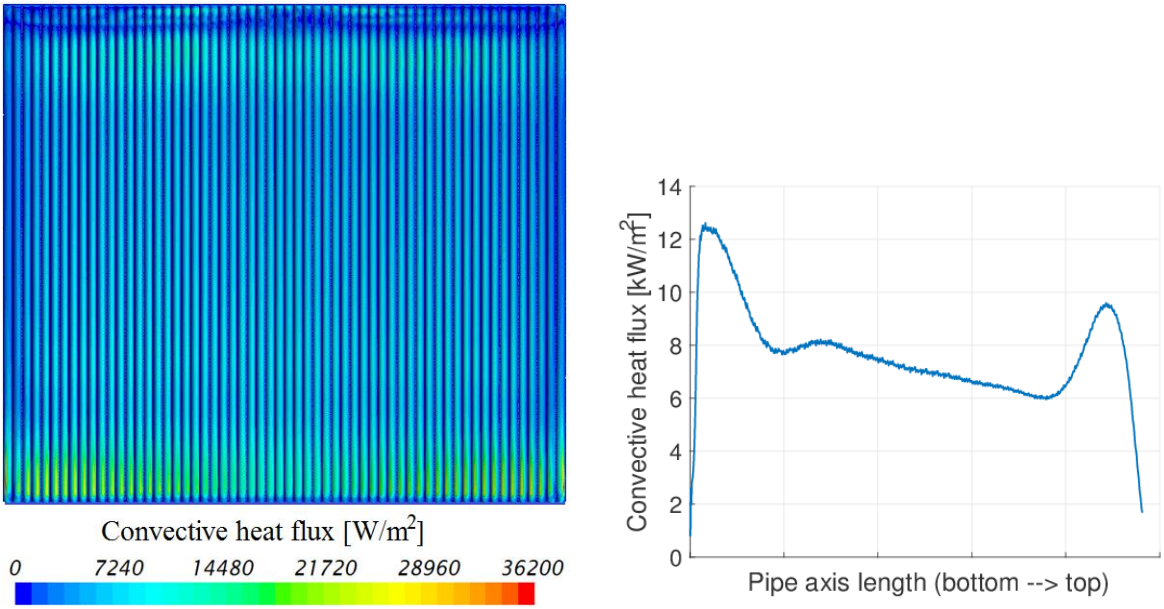

(a) (b)

Figure 11 – (a) Contours of convective heat losses from the receiver front face (tube bank) in the case of frontal wind (5 m/s) and (b) 1D axial distribution of the convective heat losses from a plane passing through the central pipe of the receiver.

4.1.2 Effect of the wind speed

In this section the effect of the wind speed on the convective losses is assessed for a given wind direction, namely the frontal direction, which allows halving the computational domain thanks to its left-right symmetry. The wind speed has been parametrically varied between 0 and 10 m/s, in order to analyze both the conditions of dominant natural convection and of dominant "forced" convection, respectively.

Figure 12 shows the results of this analysis both in terms of computed HTC and of the product of the heat transfer coefficient and the receiver area; the latter is reduced by a factor $2/\pi$ in the case of the correlations. Figure 12 also provides the comparison with the available correlations proposed by Siebers (Siebers et al., 1982), which are applicable in the range Reynolds numbers ($< 3.2 \times 10^5$) and Grashof number ($\approx 1.4 \times 10^{10}$) considered in this study. In the case of natural convection (wind speed equal to 0 m/s), the correlations largely overestimate the HTC, mainly because of the effect of the top overhang that prevents the hot air rising along the pipes to leave the receiver. According to the results of the previous section, the correlations overestimate the convective losses also in the case of mixed convection. Specifically, it can be seen that the higher the wind speed is, the higher the effect of the protection given by the external structure in the reduction of the convective heat losses; therefore, the difference between the results of the CFD model and those obtained using the correlations increases as the wind speed increases.

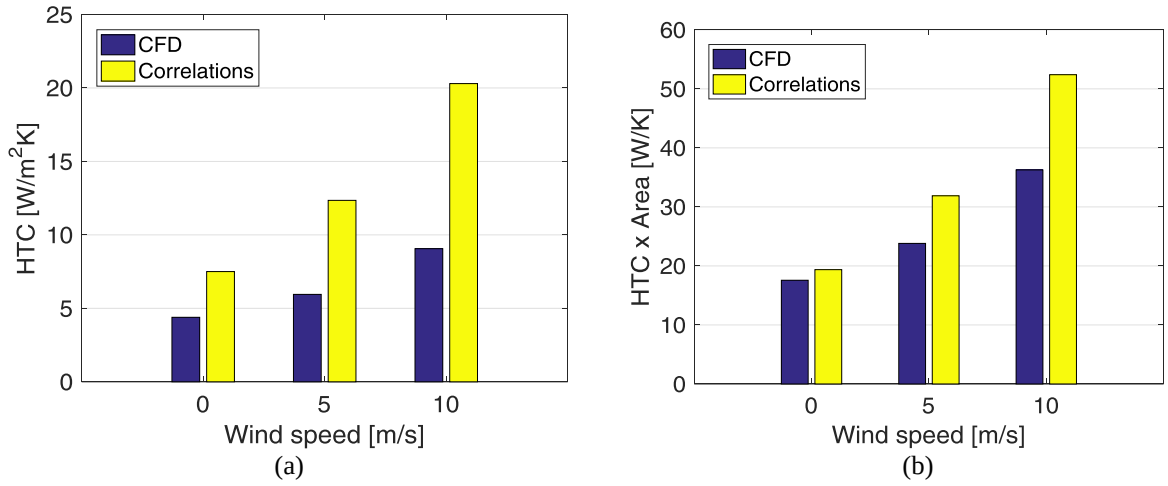

Figure 12 – Comparison between the results of the CFD model of the actual geometry and of the available correlations for different wind speeds in terms of (a) HTC and (b) HTC multiplied by the heat transfer area

The computed 2D maps of the convective heat flux from the receiver surface, in the two limiting cases of 0 and 10 m/s wind speed, are shown in Figure 13a and 9b, respectively. In the former case the integrated convective loss amounts to 10.9 kW and accounts for 11.6 % of the total heat loss (including convection, reflection and radiation), whereas in the case of 10 m/s wind the convective losses obviously increase, reaching 22.5 kW (21.2 % of the total).

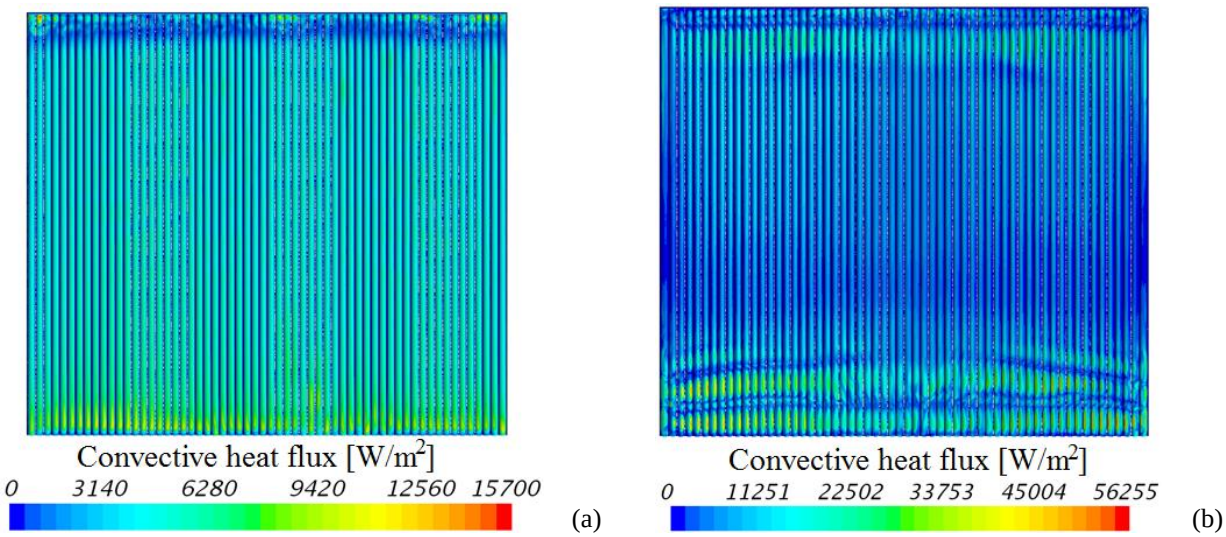

Figure 13 – Contours of convective heat losses from the receiver front face (tube bank): (a) without wind and (b) with a wind speed equal to 10 m/s (frontal direction).

The 1D (axial) distributions of the losses shown in Figure 13 is qualitatively the same of the one obtained in the case of a wind speed equal to 5 m/s (Figure 11a). In particular, peaks in the convective heat flux can be observed near to the top and bottom ends of the pipes, which are caused by the presence of vortices that locally enhance the air mixing leading to a higher convective heat transfer; see Figure 14 and Figure 15.

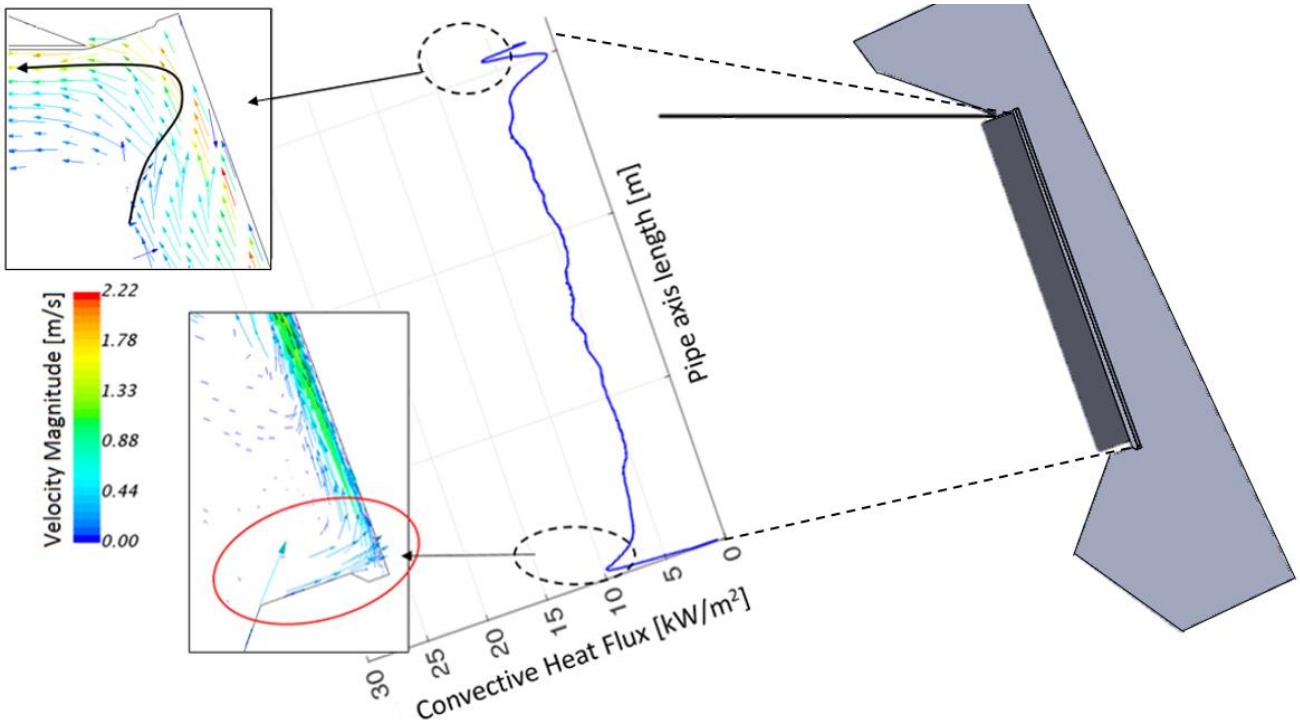

Figure 14 – 1D axial distribution of the convective heat losses from a plane passing through the central pipe of the receiver combined with the air flow field (computed on the same plane) around of the top and bottom part of the tube bank, in the case of free convection (0 m/s wind speed)

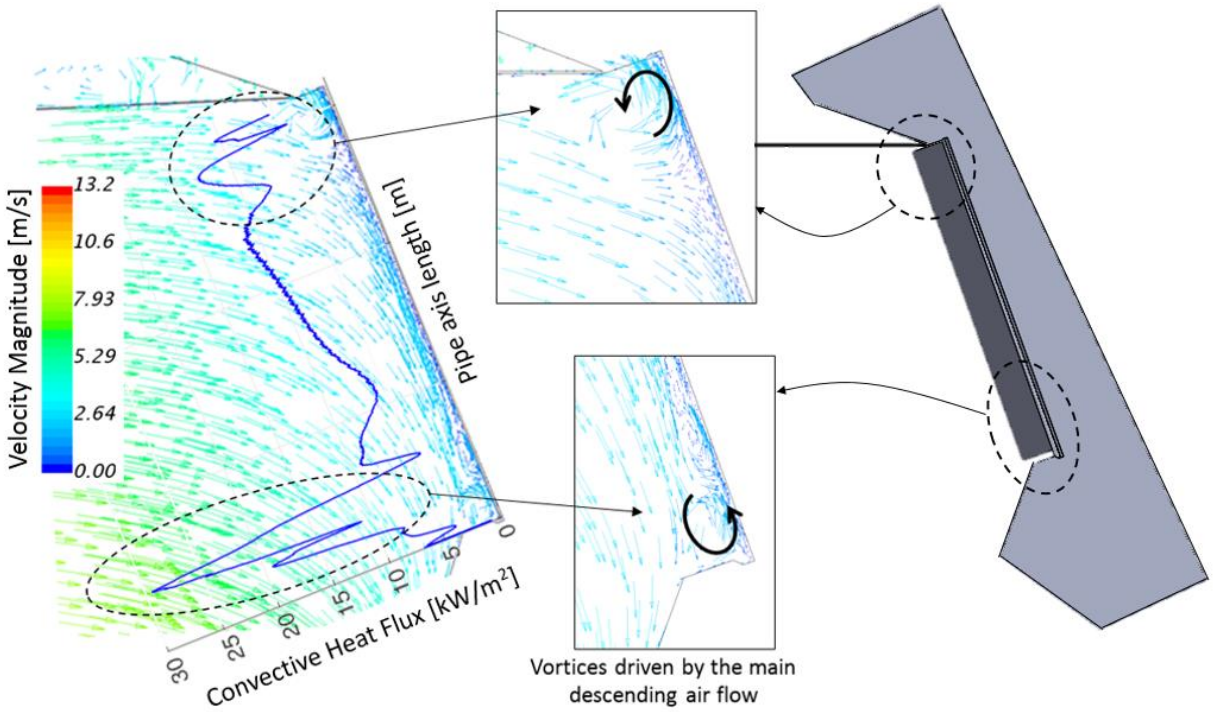

Figure 15 – 1D axial distribution of the convective heat losses from a plane passing through the central pipe of the receiver combined with the air flow field computed on the same plane (details of the flow field close to

the top and bottom part of the tube bank), in the case of a 10 m/s wind speed blowing frontally towards the tubes.

Apart from the vortex structures, the main features of the flow in the two cases are clearly recognizable: at a wind speed of 0 m/s (free convection), the flow naturally rises along the receiver surface, then impacts upon the overhang and is then redirected away from the receiver. At a wind speed of 10 m/s, the flow is mainly forced by the wind along the overhang, then downwards along the receiver, as was already observed for the case of a wind speed of 5 m/s (Figure 10b).

Table 3 summarizes the important outcomes of the CFD simulations. In particular, it may be noted that heat losses are dominated by radiation, while the convective losses account for about 10-20% in the range of wind speeds considered in this study (0-10 m/s). In order to determine the heat lost by radiation, the surface-to-surface (S2S) radiation model has been included in the CFD model, which computes the radiative heat transfer between diffuse surfaces considering the view factor between the surfaces and the surface emissivity. The latter has been assumed to be equal to 0.87 for the surface coating (Pyromark 2500) of the absorber pipes (Ho et al., 2013). Most of the radiative heat transfer from the tube bank is with the border surfaces of the external air domain, whose temperature is the ambient temperature (20 °C). The remaining share of the radiative losses is due to the heat transfer between the tube bank and the receiver external structure (top overhang and lateral wings), which is responsible for the slight change of the radiative losses with the wind speed, since the temperature of the external structure is affected by the intensity of the wind.

Table 3 – Total (convective plus radiative), convective heat losses and corresponding average heat transfer coefficient computed with the CFD model for different wind speeds

Wind speed	**0 m/s**	**5 m/s**	**10 m/s**
Total heat losses [kW]	93.8	97.9	105.9
Convective losses [kW]	10.9	14.8	22.5
Radiative losses [kW]	82.9	83.1	83.4
Convective/Total losses [%]	11.6	15.1	21.2
Average HTC [W/m^{2}K]	4.39	5.95	9.06

4.1.3 Effect of the wind direction

In the previous section, the convective and radiative heat losses have been numerically evaluated for different wind speeds and different thermal drivers (imposed uniform temperature and imposed heat fluxes), but considering only one wind direction (see section 3.1). Specifically, the direction parallel to the ground and symmetric with respect to the receiver face, i.e., the so-called "frontal" direction. In the present section, we present the results of the CFD analysis at different wind directions (0^o - frontal, 30^o, 60^o - tangent to one of the wings, 75^o and 180^o), for a given (5 m/s) wind speed and a uniform pipe surface temperature (634 °C). The resulting flow fields in the horizontal plane passing through the center of the receiver surface are shown in Figure 16.

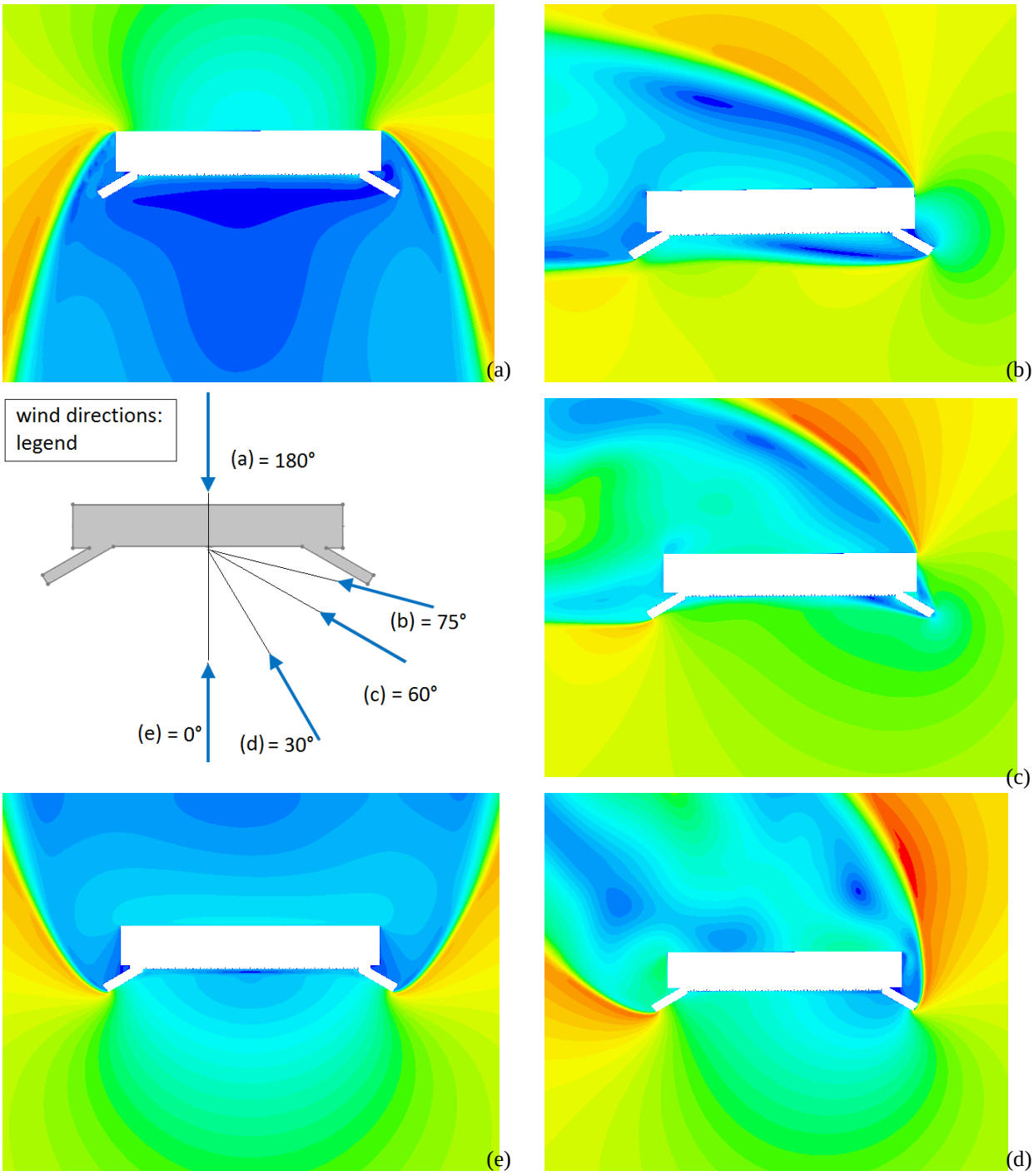

Figure 16 – Contours of the computed air speed on the horizontal mid-plane of the tube bank, for different wind directions: (a) 180°, (b) 75°, (c) 60° - tangent to one of the wings, (d) 30°, (e) 0° - frontal. The (imposed) wind speed is equal to 5 m/s in all cases.

Figure 16 shows that the average air speed close to the absorber hot pipes increases moving from 0° (frontal direction) to 60° (wind tangent to one of the wings), since the wind direction becomes more glancing to the tube

bank. This, in principle, should imply that the heat transfer is enhanced when the incidence angle increases from 0º towards 60°.

The increase of the air speed moving from 0° to 60° can be also quantitatively observed in Figure 17, which shows the velocity magnitude along a line normal to the tube bank, through its center. With a wind direction characterized by an angle higher than 60°, particularly in the range 60-90°, part of the tube bank is protected against the direct wind by one of the wings that acts as a barrier. This is the case of the wind direction equal to 75° (Figure 16b).

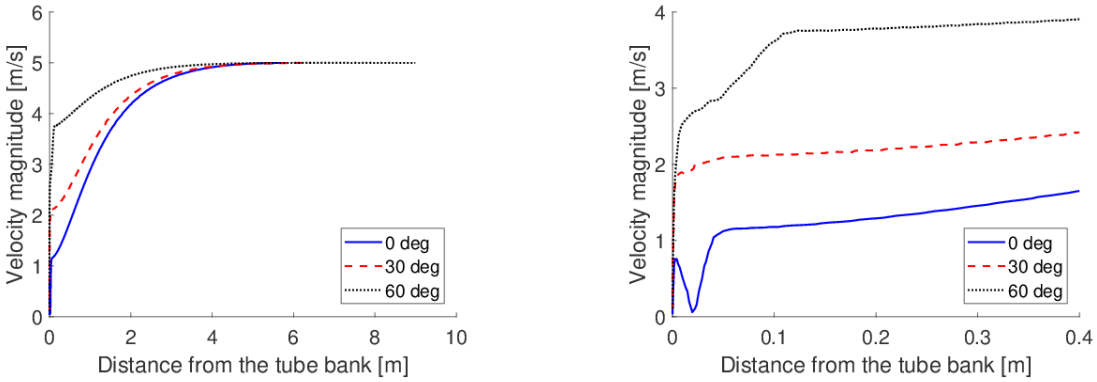

(a) (b)

Figure 17 – (a) Computed velocity magnitude along a line normal to the tube bank through its center and (b) zoom on the zone close to the tube bank. The unperturbed wind speed is imposed equal to 5 m/s and the pipe surface temperature is set equal to 634 °C.

However, the main air stream drives a vortex structure (shown in Figure 18a) that potentially improves the air mixing close to the hot absorber pipes enhancing the heat transfer. Finally, if the wind blows from behind the receiver (180°), the front of the receiver tubes is characterized by very low speeds, as seen in Figure 16a, due to the shedding of vortices off the receiver structure (Figure 18b), . However, note that this is a result of a steady-state simulation, and transient vortex shedding (a Karman vortex street) may be seen in reality with somewhat higher time-averaged heat transfer.

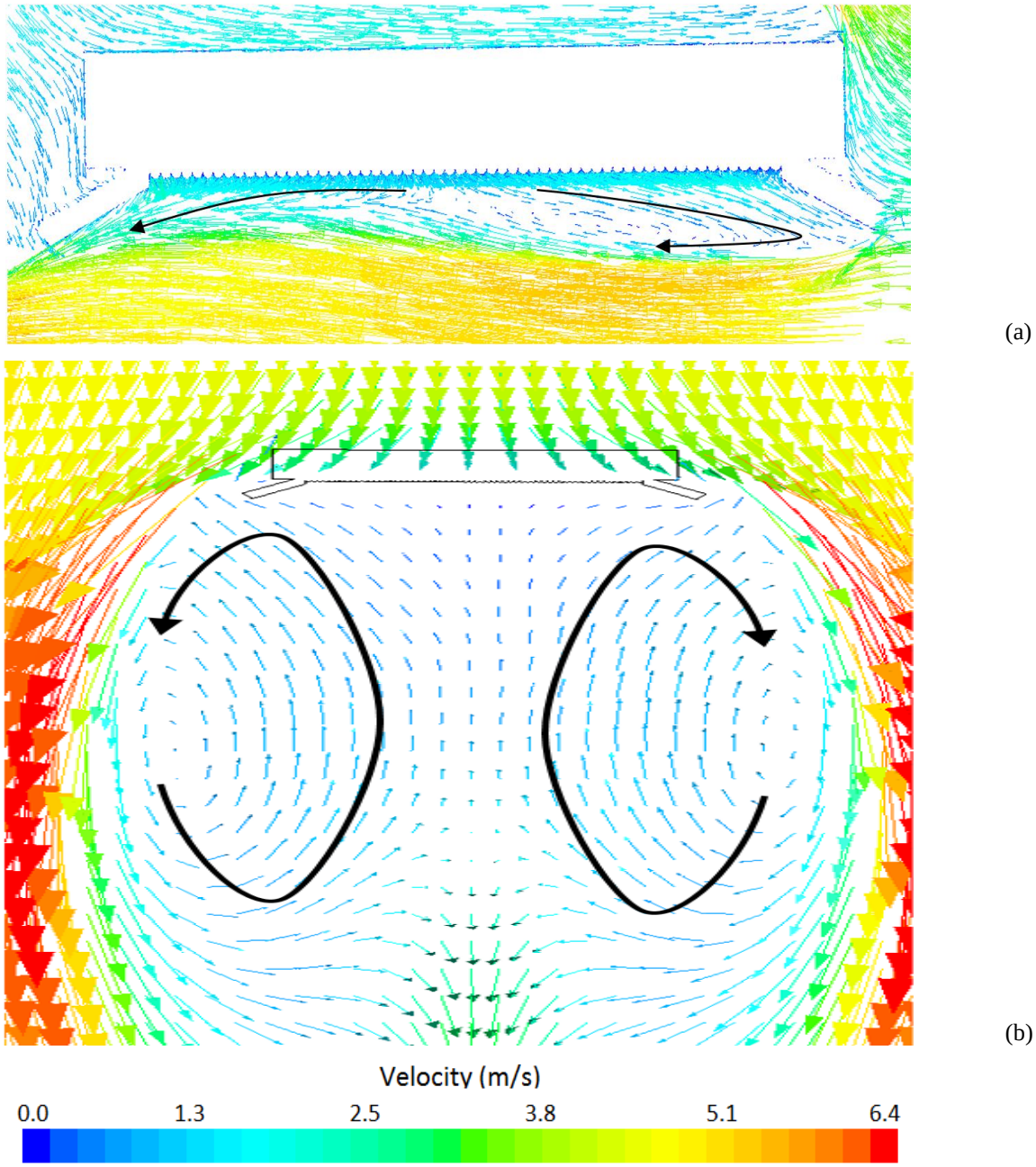

Figure 18 – Velocity vectors on the horizontal mid-plane of the tube bank in the case of wind direction equal to (a) 75° and (b) 180°, for a given wind speed (5 m/s)

The corresponding variation of the convective heat loss is shown in Figure 19. It is seen that the convective losses increase from 0° to 60° as a results of the higher air speed close to the hot pipes. The vortex identified in Figure 18a for a wind direction of 75° leads to an effective air mixing close to the receiver surface resulting in a convective heat loss even higher than the one obtained for the case of the wind blowing tangent to one of the wings. The minimum value is obtained in the case of the wind blowing from the receiver backside (180°) since the hot pipes are shielded from the direct air stream, and the forced convective losses in this case are caused by the vortices released on the downwind side of the receiver. Note that these vortices lead to convective heat losses comparable with those obtained in the case of wind blowing frontally to the receiver face, where a region of relatively low air speed was detected in front of the tube bank (see Figure 16a) as a consequence of the cavity-like behavior discussed previously in this section.

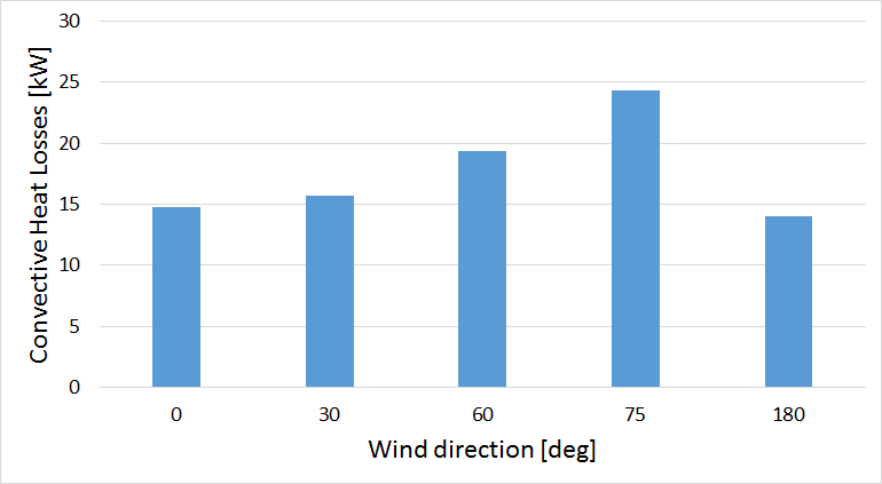

Figure 19 – Convective heat loss computed by the CFD analysis as a function of the wind direction (0º - frontal, 30º, 60º - tangent to one of the wings, 75º, 180º) for given wind speed equal to 5 m/s.

4.2 Imposed incident heat flux (non-uniform pipe surface temperature)

A realistic, non-uniform temperature distribution to drive the CFD receiver model can be obtained from experiments, or from other models. In this Section, the latter approach has been adopted and the system-level model, developed to simulate the JSTS at the system level, as presented in Section 2, was used. The wind speed in this analysis is set to 5 m/s and the ambient air temperature is fixed at 20 °C. Since the surface temperature distribution and the convective losses have mutual interactions, an iterative procedure is adopted to determine each self-consistently, as shown in the flow chart of Figure 20.

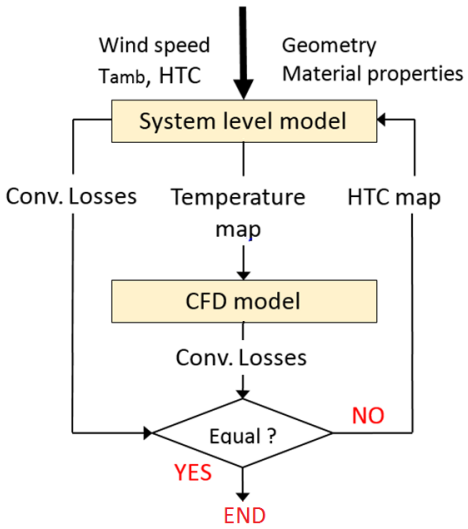

Figure 20 – Scheme of the iterative procedure applied to combine the CFD model (external air flow) with the lumped-parameter model (internal sodium flow)

The procedure can be explained as follows:

1. Compute the temperature distribution using the system-level model, with a first-guess, average external HTC of ~13.5 W/m^{2}K, estimated from correlations in the literature (Eqs. 8-10);
2. Import this temperature distribution in the CFD model, which in turns evaluates the convective heat losses and consequently, as a post-processing result, the distribution of the HTC;
3. Run again the system-level model with the new local HTC obtained from the CFD model, in order to determine a new temperature distribution.

The iterations reach convergence when the CFD model and the system-level model provide the same convective losses, within a reasonable tolerance. In the case considered here, the procedure converges very quickly and in three iterations one reaches the asymptotic value $Q_{conv} \approx 10.5$ kW that correspond to an average HTC of about 6.5 W/m^{2}K. The convergence should be fast both in the case of forced and in the case of natural convection, because the wall temperature distribution in mainly determined by the solar heat flux distribution, by the internal convection and by the external radiation, which dominates the heat losses. Figure 21b shows the surface temperature distribution obtained from the system-level model at the end of the iterative process. This distribution is an obvious consequence of the incident heat-flux distribution (shown in Figure 21a), and of the upward flow of the sodium HTF. With respect to the incident heat, a normal heat-flux distribution is assumed with a standard deviation equal to $0.255 \times L$ (Boerema et al., 2013) where L is the length of the receiver, while the total incident power is equal 1.2 MW (Coventry et al., 2015). The 2D heat flux map (Figure 21a) is discretized in the system-level model in a 20x20 grid.

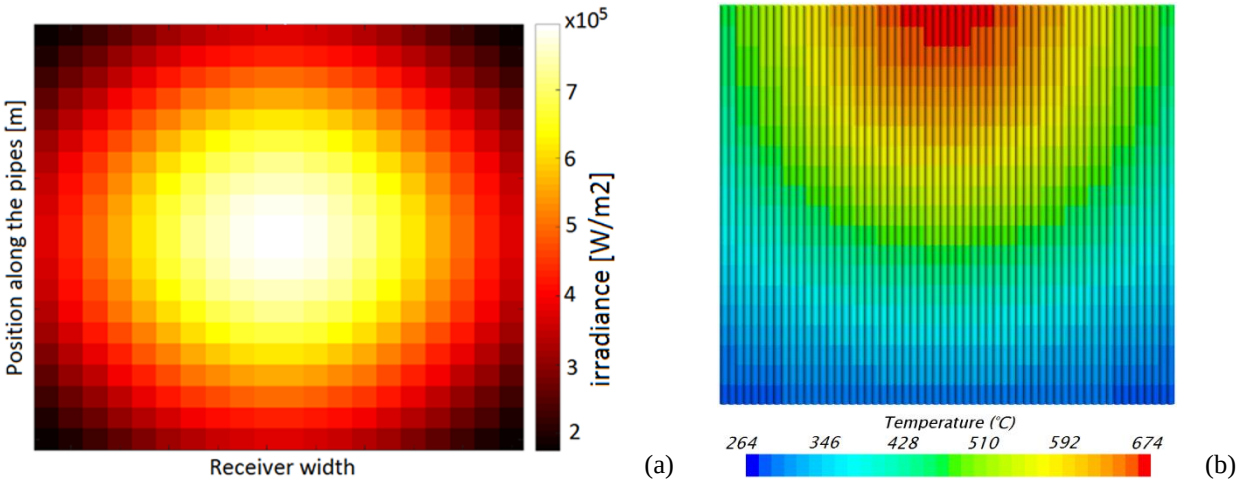

Figure 21 – (a) Distribution of the incident heat flux on the absorber surface. (b) Computed temperature distribution (at the end of the iterations) on the absorber surface. Wind speed = 5 m/s.

The distribution of the convective heat loss (Figure 22 right) is affected by the surface temperature distribution and by the distribution of the HTC (Figure 22 left), which is in turn affected by the air flow in front of the receiver. An increase of the air speed determines a local increase in the convective HTC (circled regions in Figure 22 right) and consequently in the heat losses by convection. The temperature is also high in the top circled regions, not just the HTC, therefore the convective heat loss peaks there.

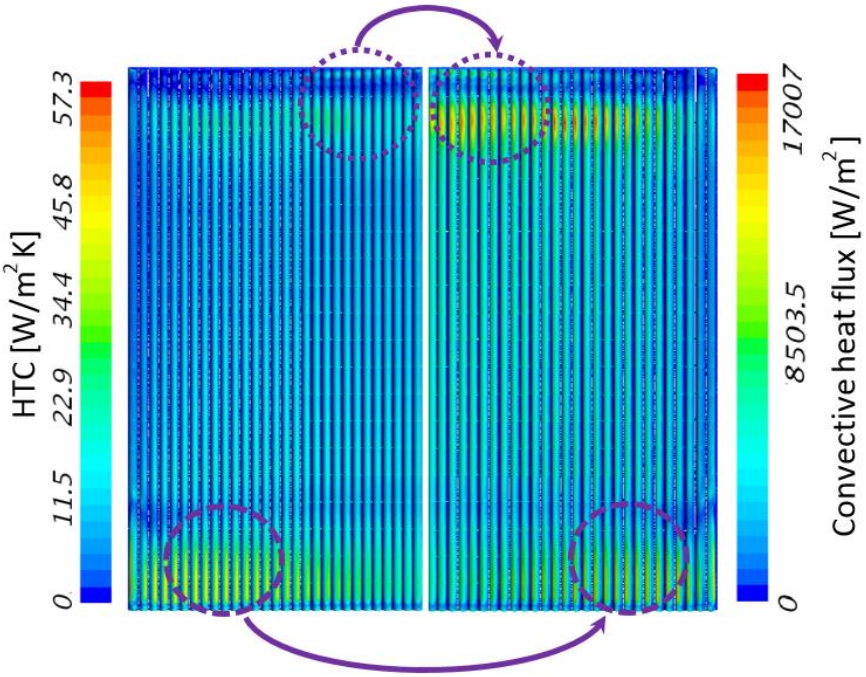

(a) (b)

Figure 22 – (a) Computed distribution of the convective HTC on the absorber pipes surface obtained post-processing the CFD results and (b) resulting convective losses with the CFD model. Each of the 2D maps shows only half of the receiver surface, the left and the right one, respectively, due to the full symmetry of both geometry and boundary conditions (wind blowing frontally toward the pipes).

5 Results of the system-level model and discussion

5.1 Benchmark vs. the Boerema model

To first prove the reliability of the new receiver model, a benchmark analysis was carried out (Table 4) considering a similar model developed and validated against experimental data by (Boerema et al., 2013). To this purpose, the receiver model parameters (e.g., pipes dimensions, incident power, etc.) were set according to the ones adopted in Boerema et al. (2013). In particular, the same constant external heat transfer coefficient, equal to 16 W/m^{2}K, was imposed, and the sodium mass flow rate was set to ensure the same enthalpy jump across the pipes. The results in Table 4 show a relatively small discrepancy (≈ 5%) in the radiative plus convective heat loss calculated by the two models, which indicates a difference in the computed temperature distribution of the outer receiver surface. This deviation is likely a result of the differences between the two models, which include the correlation adopted to compute the inner heat transfer coefficient between sodium and pipes, and the axial heat conduction that is neglected in the Boerema model. Moreover, in the Boerema model the irradiated side of the pipe is discretized also along the azimuthal direction, while in the model presented here a coarse azimuthal discretization is considered, which only divides the irradiated and the back side of the pipe. The receiver efficiency computed with the new model is equal to 91.4%, while it is 91.2% in (Boerema et al., 2013), confirming the very good agreement between the two models.

Table 4 – Comparison of the new receiver model with Boerema et al., (2013).

Losses	New receiver model	Boerema et al. (2013)
Optical [kW]	95.5	95.5
Radiative [kW]	32.8	50.4 [a]
Convective [kW]	15.1	
Total [kW]	143.4	145.9

[a] Only the sum of the convective and radiative heat losses is provided.

5.2 Preliminary validation vs. experimental data

The model has been validated against experimental data provided by Vast Solar. Among these data, the Na inlet temperature and flow rate, the wind speed and ambient temperature, and the DNI-based heat flux *estimation* (see below) are used in input to the code, whereas the Na outlet temperature is used to validate the model output.

The above-mentioned heat flux estimation is obtained as follows

$$Q_{DNI} = DNI \times \eta_{opt} \tag{16}$$

where η_{opt} = 0.9 is a roughly estimated optical efficiency of the solar field and Q_{DNI} is the DNI-based heat flux estimation. As some residual uncertainties remain concerning the actual optical efficiency of the field, the Pyromark coating absorptivity (which may vary between ~ 0.88 for a degraded coating (Ho et al., 2013) and ~ 0.95, design value), and the calibration state of the pyrheliometer, a parameter β is then introduced to define the incident heat flux (Q_{in}) to be used as driver in our analysis as follows

$$Q_{in} = \beta \times Q_{DNI} \tag{17}$$

Next, β is varied parametrically, searching for the value that best fits the steady state. For an assumed coating absorptivity = 0.88, the best fit of the normalized average outlet Na temperature (defined as the ratio between the actual temperature and the average temperature measured at quasi steady-state conditions, i.e., during the central hours of the day) is achieved with β = 0.79. This value is then kept constant during the entire transient analysis.

The results of the comparison between simulation and measurement are presented in Figure 23, where a very good agreement is achieved for the whole transient considering also the uncertainties in the measured DNI, temperatures and mass flow rate as communicated by Vast Solar.

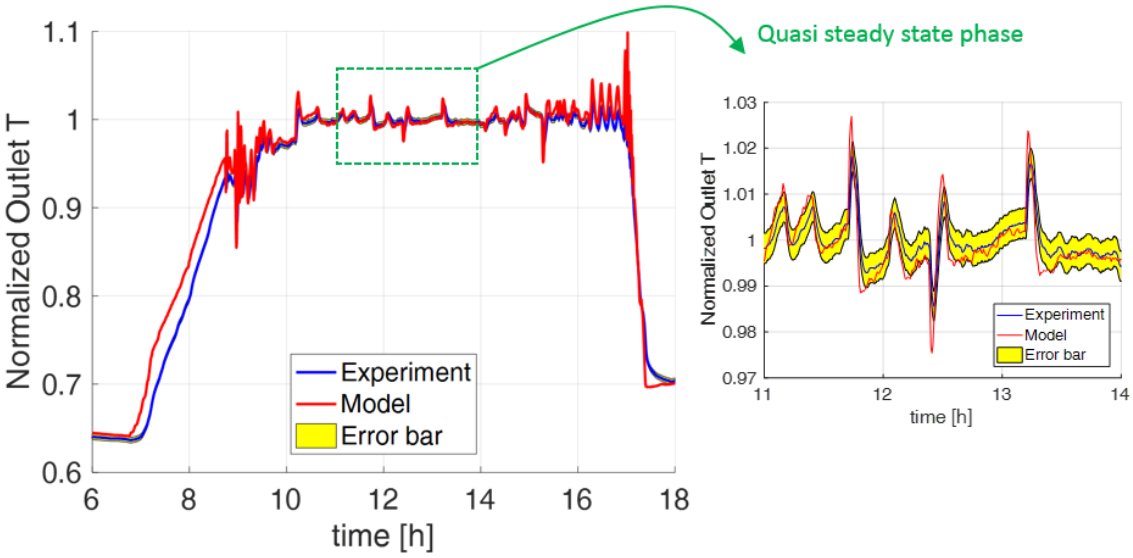

Figure 23 – Model validation against experimental data: comparison between computed and measured evolution of the sodium outlet temperature. The error bar takes into account the uncertainties in the measured DNI, temperatures and mass flow rate.

5.3 Application to a fast transient (start-up/passing cloud/shut-down)

The transient considered here is shown in Figure 24 (top left part). The system to which the transient is applied consists of the receiver only (Figure 24, right part). That is, the model is used in a standalone mode as no circuit is included. Boundary conditions are provided by a source/sink pair: the former prescribes a given inlet sodium mass flow rate, at a given temperature (270 °C), such that $T_{out} = 560$ °C at plateau (no control); the latter imposes the outlet pressure, set equal to about 1 bar. The wind speed is set to 5 m/s, which we showed (above) to be a reasonable average value for the weather data available, and the ambient temperature is assumed to be 20 °C. The applied thermal driver consists of a 2D heat flux map (Figure 21a), which is then switched on and off according to a square wave signal to simulate plant start-up, steady-state operation interrupted by a cloud passing, and finally plant shut-down. Similarly to Section 4.2, the heat flux map has been discretized using a 20×20 grid. The passing cloud is assumed to act instantaneously in taking the incident heat to zero; the off-sun condition is kept for the entire transit time of the cloud (30 s), then the incident heat is suddenly switched on again. This is a worst-case scenario since most clouds have a velocity such that they will take of the order of several seconds to pass across the field, and also they have a gradient in opacity that leads to a smoother ramping up and down of the incident heat. The time between the start-up and the cloud arrival and the time between the cloud leaving and the plant shut-down has been chosen in order to ensure that steady-state conditions have been achieved.

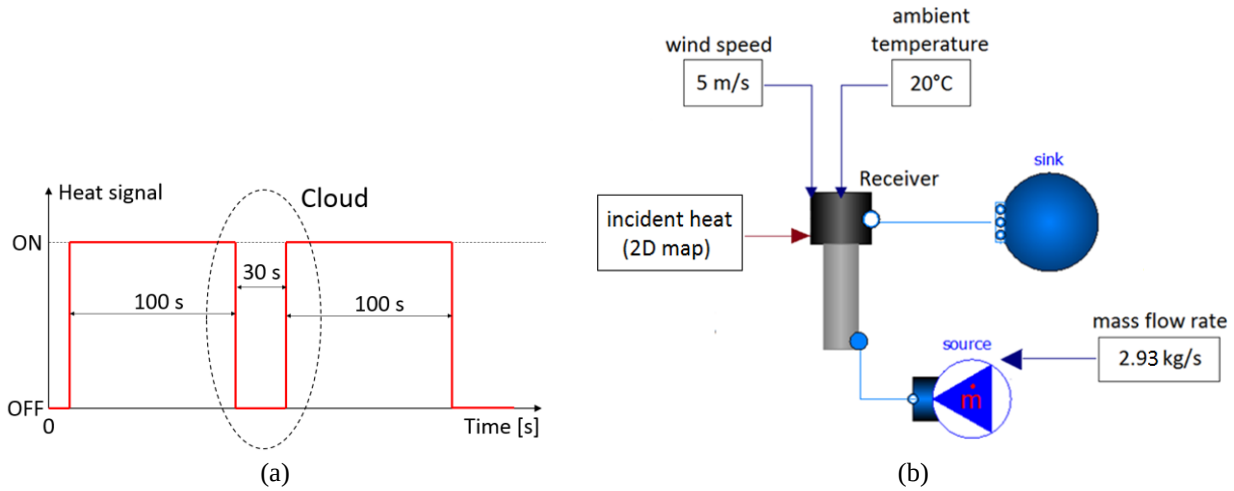

(a) (b)

Figure 24 – Passing cloud transient, simulated by means of a square-wave signal that switches off/on the incident heat (a). Sketch of the standalone receiver model with boundary conditions (b).

The results of the analysis are presented in Figure 25. The response of the sodium outlet temperature to a variation of the incident heat takes about 1 minute. The transient duration is dominated by the thermal capacity of the pipe wall. The fast transient given by the passing cloud shows that the sodium temperature suddenly decreases, almost approaching the inlet temperature in the 30 seconds of the transient. This suggests that the implementation of a control strategy is mandatory in order to avoid high oscillations in the outlet temperature. As highlighted in the inset of Figure 25, the outer surface temperature of the pipes is higher than the temperature T_w in the middle of the pipe thickness only as long as the receiver is irradiated, while it suddenly becomes lower than T_w as soon as the irradiation goes to zero, because of the passing cloud. This instantaneous reduction of the outer wall temperature is clearly non-physical, since the outer surface needs in reality a finite time to change its temperature, and it is due to the fact that all the mass of the wall is lumped in the middle of the pipe thickness, where the time derivative of the wall temperature is computed (see Eq. 1). However, for real (not instantaneous) transients, this feature of the model should not significantly affect the accuracy of the results. The receiver model also provides the rate of change of the wall temperature during the transient, which is a meaningful parameter for an eventual thermal stress analysis; in the case simulated here, the maximum value reached is about 34 °C/s. This result demonstrates the ability of this model to predict realistic thermal transients; it is anticipated that control strategies will need to be applied to greatly reduce these transients during normal operation of the plant.

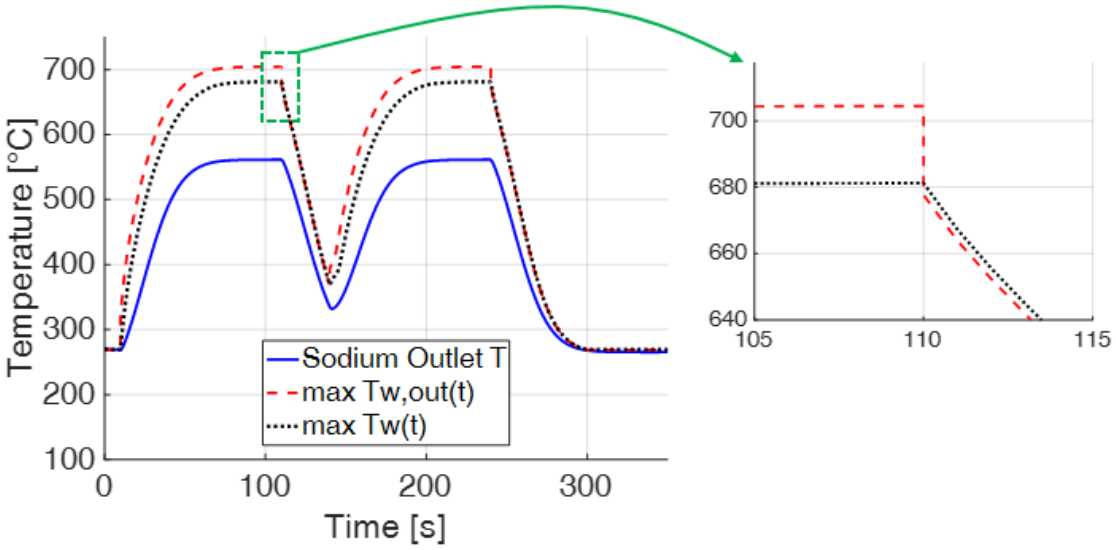

Figure 25 – Computed evolution of the sodium outlet temperature, and the maxima of the wall temperature (T_w -- middle of the wall section) and outer surface temperature ($T_{w,out}$) across the entire receiver surface.

5.4 Whole-day simulation

To thoroughly test the compatibility of the new receiver model with the SolarTherm library, the receiver model was incorporated into a full reference system model, depicted in Figure 2, which includes all the main components of a central receiver plant. In this environment, sodium is used in the receiver hydraulic loop and as storage medium. At the receiver level, the main difference with respect to the simplified model previously presented in Figure 24 consists in the modelled control system that ensures an almost-constant outlet temperature, equal to the design value (560 °C), during the whole day. This is obtained by regulating the sodium mass flow rate trough the receiver according to the irradiance value; in particular, a proportional–integral controller (PI) is adopted, which exploits a control loop feedback mechanism based on the outlet temperature

The whole day simulation was set-up considering a plant located close to Alice Spring, Australia, and the weather data for the first day of the year according to the weather available as part of the SolarTherm library. The simulation was run from sunrise to sunset. Since the current version of the SolarTherm Library only allows driving the new receiver model with the total power incident on it (i.e. it cannot impose a 2D heat flux map), a uniform heat flux distribution on the receiver surface was assumed for the purposes of this exercise.

Figure 26 shows that the mass flow rate evolution during the day follows a trend similar to that of the incident power; qualitatively, the ratio between the two turns out to be approximately constant, whereas quantitatively the specific enthalpy increase is almost exactly constant, as enforced by the action of the control system. The small variations of the ratio between the incident heat and the mass flow rate are due to the heat losses that change during the day depending on the ambient temperature and wind speed.

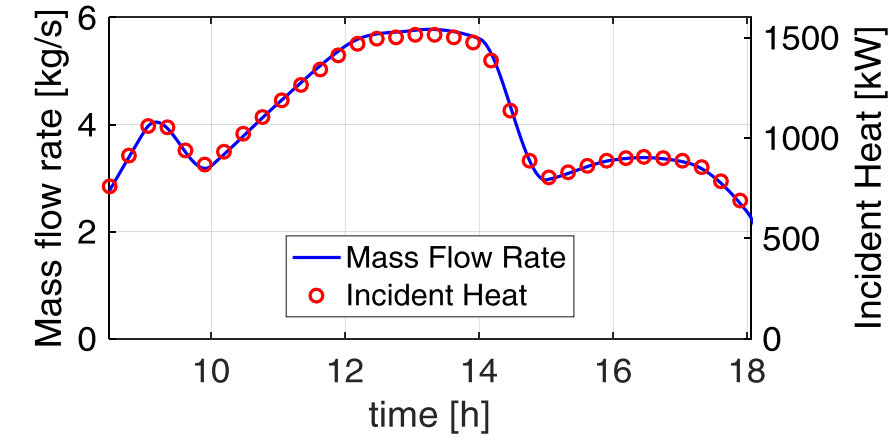

(a)

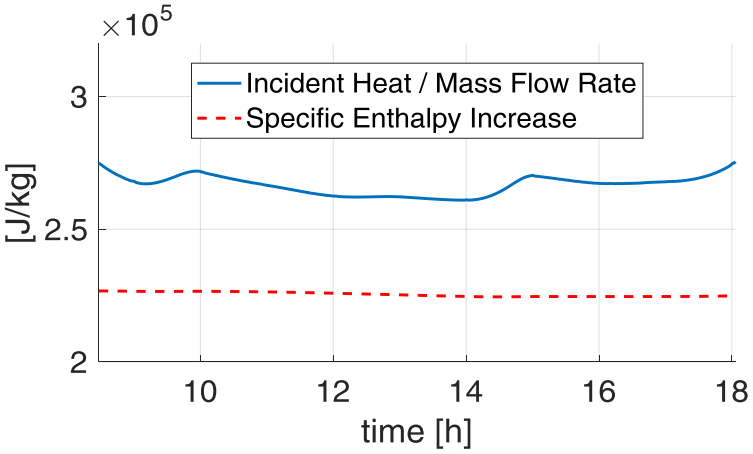

(b)

Figure 26 – Whole day simulation: (a) mass flow rate + incident heat and (b) ratio between the incident heat and the mass flow rate (solid line) and specific sodium enthalpy increase (dashed line). The gap between the two curves corresponds to the heat losses plus the optical losses due to the not perfect absorptivity of the surface coating.

The receiver thermal efficiency, which is defined as

$$\eta = \dot{m}\,(h_{out} - h_{in})/Q_{in} \tag{18}$$

oscillates from 83% to 87% according to the trend of the incident power, i.e., it is quite constant throughout the entire day.

6 Conclusions and perspective

A dynamic model for billboard-type sodium-cooled receivers was developed in the Modelica language.

The new receiver model is supported by a detailed 3D CFD analysis, which was performed for different wind speeds at given (frontal) direction, as well as for different directions at given (5 m/s) wind speed. The CFD model permits analysis of the actual geometry of the receiver, which affects the air flow close to the absorber surface and therefore, directly, the convective heat losses; thus, this approach aims improving the accuracy of the results where the geometry considered in the available empirical correlations is just a poor approximation of the actual receiver shape. First, the CFD model has been compared with the available correlations in the case described by the correlations,

namely the flat plate in parallel flow, obtaining a very good agreement. A cavity-like behaviour has been noted in the flow field computed in front of the hot absorber pipes, which is determined by the receiver structure (wings and top overhang). A series of CFD models of increasing complexity allowed us to conclude that the cowling was responsible for most of the difference between our CFD results and the predictions for heat loss from a vertical flat panel, and detailed discussion of the flow structure was given in support of this finding. The analysis performed suggests that the convective losses can be reduced by ≈ 25% due to the presence of the cowling.

Moving from the case of the absence of wind (free convection) to the case of dominant forced convection (wind speed equal to 10 m/s), the convective heat losses double, but they still represent a small fraction (≈ 20%) of the total heat losses, which remain dominated by radiation. The flow field, for each of the wind speeds considered here, is characterized by vortices close to ends of the pipes that locally enhance the heat transfer, despite the overall beneficial effect of the cowling

The wind direction has been observed to strongly affect the convective heat loss, which increases as the wind direction becomes more glancing to the tube bank. The maximum of the convective losses corresponds to a wind direction between the tangent to one of the wings (60°) and the direction parallel to the tube bank (90°); in this case a vortex structure has been identified close to the tube surface that effectively increases the air mixing leading to relatively high convective losses.

The new dynamic receiver model was partly verified by comparing the results obtained in steady-state conditions with those calculated by Boerema using a similar model, assuming the same geometry and boundary conditions. A further validation of the model was then carried out against dynamic experimental data. The computed outlet temperature in quasi steady-state conditions turns out to compare very well with the measurements, within the uncertainties of the input data. In perspective, this validation should be extended focusing on dynamic conditions and (as far as is possible) reducing the uncertainties in the incident heat data.

A first application of the receiver model to a fast transient (passing cloud) has been presented, which shows qualitatively reasonable results. Moreover, a whole-day plant-scale simulation has been presented, confirming the complete compatibility of the new receiver model with the SolarTherm Modelica library.

This study is expected to act as the base for further developments. For example, the 3D CFD model should be exploited to derive a correlation for the external heat transfer coefficient, taking into account the tube external temperatures and the wind direction and speed, or could be adapted to different tube layouts on the receiver surface. In addition, the full validation of the CFD model against experimental data could be an interesting task to be addressed. Finally, the SolarTherm library, equipped with the new receiver model, could be used to study the effect of different control strategies on the plant performance as well as to identify possible hot spots due to the uneven heat flux distribution.

Acknowledgments

We thank Vast Solar for kindly providing the needed input for the analysis of the JSTS receiver. P. Giomi and L. Vancheri contributed to the initial part of the work on the system-level and CFD models, respectively, within the framework of their MSc thesis at Politecnico di Torino. The work of AdlC and JP was performed as part of the Australian Solar Thermal Research Initiative (ASTRI), a project supported by the Australian Government, through the Australian Renewable Energy Agency (ARENA).

References

Abbott, D., 2010. Keeping the energy debate clean: How do we supply the world's energy needs?, in: Proceedings of the IEEE. pp. 42–66. doi:10.1109/JPROC.2009.2035162

Australian Government – Bureau of Meteorology, 2018. Meteo Data [WWW Document]. URL http://www.bom.gov.au/climate/averages/tables/cw_065016.shtml

Ávila-Marín, A.L., 2011. Volumetric receivers in Solar Thermal Power Plants with Central Receiver System technology: A review. Sol. Energy 85, 891–910. doi:10.1016/j.solener.2011.02.002

Behar, O., Khellaf, A., Mohammedi, K., 2013. A review of studies on central receiver solar thermal power plants. Renew. Sustain. Energy Rev. 23, 12–39. doi:10.1016/j.rser.2013.02.017

Boerema, N., Morrison, G., Taylor, R., Rosengarten, G., 2013. High temperature solar thermal central-receiver billboard design. Sol. Energy 97, 356–368. doi:10.1016/j.solener.2013.09.008

Boerema, N., Morrison, G., Taylor, R., Rosengarten, G., 2012. Liquid sodium versus Hitec as a heat transfer fluid in solar thermal central receiver systems. Sol. Energy 86, 2293–2305. doi:10.1016/j.solener.2012.05.001

Casella, F., Leva, A., 2006. Modelling of thermo-hydraulic power generation processes using Modelica. Math. Comput. Model. Dyn. Syst. 12, 19–33. doi:10.1080/13873950500071082

Cochran, T.B., Feiveson, H.A., Patterson, W., Pshakin, G., Ramana, M.V., Schneider, M., Suzuki, T., Hippel, F.V., 2010. Fast Breeder Reactor Programs: History and Status, International Panel on Fissile Materials.

Coventry, J., Andraka, C., Pye, J., Blanco, M., Fisher, J., 2015. A review of sodium receiver technologies for central receiver solar power plants. Sol. Energy. doi:10.1016/j.solener.2015.09.023

De la Calle, A., Bayon, A., Hinkley, J.T., Pye, J., 2017. System-level simulation of a novel solar power tower plant based on a sodium receiver , PCM storage and sCO2 power block, in: SolarPACES 2017 Conference Proceedings. Santiago, Chile.

Edman, J., Windahl, J., 2015. Dynamic Modeling of a Central Receiver CSP System in Modelica. Proc. 11th Int. Model. Conf. 585–594. doi:10.3384/ecp15118585

Fiebig, M., 1998. Vortices, generators and heat transfer. Chem. Eng. Res. Des. 76, 108–123. doi:10.1205/026387698524686

Haaland, S.E., 1983. Simple and Explicit Formulas for the Friction Factor in Turbulent Pipe Flow. J. Fluids Eng. 105, 89. doi:10.1115/1.3240948

Habchi, C., Russeil, S., Bougeard, D., Harion, J.L., Lemenand, T., Della Valle, D., Peerhossaini, H., 2012. Enhancing heat transfer in vortex generator-type multifunctional heat exchangers. Appl. Therm. Eng. 38, 14–25. doi:10.1016/j.applthermaleng.2012.01.020

Ho, C.K., Mahoney, A.R., Ambrosini, A., Bencomo, M., Hall, A., Lambert, T.N., 2013. Characterization of Pyromark 2500 Paint for High-Temperature Solar Receivers. J. Sol. Energy Eng. 136, 014502. doi:10.1115/1.4024031

IEA, 1986. The IEA/SSPS Solar Thermal Power Plants - Facts and Figures - Volume 1: Central Receiver Systems.

Kolb, G.J., 1994. Evaluation of power production from the solar electric generating systems at Kramer Junction: 1988 to 1993 (Report No. SAND94-2909C). Albuquerque, New Mexico, USA.

Logie, W.R., Pye, J.D., Coventry, J., 2018. Thermoelastic stress in concentrating solar receiver tubes: A retrospect on stress analysis methodology, and comparison of salt and sodium. Sol. Energy 160, 368–379. doi:10.1016/j.solener.2017.12.003

Marocco, L., Cammi, G., Flesch, J., Wetzel, T., 2016. Numerical analysis of a solar tower receiver tube operated with liquid metals. Int. J. Therm. Sci. 105, 22–35. doi:10.1016/j.ijthermalsci.2016.02.002

Modelica Association, 2018. Modelica and the Modelica Association [WWW Document]. URL https://www.modelica.org/ (accessed 2.7.18).

Niedermeier, K., Flesch, J., Marocco, L., Wetzel, T., 2016. Assessment of thermal energy storage options in a sodium-based CSP plant. Appl. Therm. Eng. 107, 386–397. doi:10.1016/j.applthermaleng.2016.06.152

Pacio, J., Marocco, L., Wetzel, T., 2015. Review of data and correlations for turbulent forced convective heat transfer of liquid metals in pipes. Heat Mass Transf. 51, 153–164. doi:10.1007/s00231-014-1392-3

Pye, J., Zheng, M., Asselineau, C.-A., Coventry, J., 2015. An exergy analysis of tubular solar-thermal receivers with different working fluids. Proc. SolarPACES Conf. Beijing, 2014.

Rockwell International, 1983. Sodium Solar Receiver Experiment - Final Report. Report No. SAND82-8192.

Rodríguez-Sánchez, M.R., Soria-Verdugo, A., Almendros-Ibáñez, J.A., Acosta-Iborra, A., Santana, D., 2014. Thermal design guidelines of solar power towers. Appl. Therm. Eng. 63, 428–438. doi:10.1016/j.applthermaleng.2013.11.014

Romero, M., González-Aguilar, J., 2017. Advances in Concentrating Solar Thermal Research and Technology. doi:10.1016/B978-0-08-100516-3.00007-1

Scott, P., De la Calle, A., Hinkley, J.T., Pye, J., 2017. SolarTherm: A flexible Modelica-based simulator for CSP systems, in: AIP Conference Proceedings. doi:10.1063/1.4984560

Siebers, D.L., Moffatt, R.F., Schwind, R.G., 1985. Experimental, Variable Properties Natural Convection From a Large, Vertical, Flat Surface. J. Heat Transfer 107, 124–132.

Siebers, D.L., Moffatt, R.F., Schwind, R.G., 1982. Experimental mixed convection from a large, vertical plate in a horizontal flow, in: In 7th International Heat Transfer Conference. Munich, West Germany.

Torres, J.F., Ghanadi, F., Nock, I., Arjomandi, M., Pye, J., 2018. Mixed convection around a tilted cuboid with an isothermal sidewall at moderate Reynolds numbers. Int. J. Heat Mass Transf. 119, 418–432. doi:10.1016/j.ijheatmasstransfer.2017.11.109

Vast Solar, 2018. Vast Solar Group [WWW Document]. URL http://www.vastsolar.com/ (accessed 2.2.18).

Zanino, R., Bonifetto, R., Christian, J.M., Ho, C.K., Richard, L.S., 2013. Effects of RANS-type turbulence models on the convective heat loss computed by CFD in the solar two power tower, in: Energy Procedia. pp. 569–578. doi:10.1016/j.egypro.2014.03.061

Zhang, J.B., Valle-Marcos, J.C., El-Hefni, B., Wang, Z.F., Chen, G.F., Ma, G.C., Li, X., Soler, R., 2013. Dynamic simulation of a 1MWe concentrated solar power tower plant system with Dymola®, in: Energy Procedia. pp. 1592–1602. doi:10.1016/j.egypro.2014.03.168